Computational modeling of AMPK and mTOR crosstalk in glutamatergic synapse calcium signaling

A. Leung[1], and P. Rangamani[2,*]

[1]Chemical Engineering Graduate Program, University of California San Diego, La Jolla, CA, USA

[2]Department of Mechanical and Aerospace Engineering, University of California San Diego, La Jolla, CA, USA

[*]To whom correspondence must be addressed – prangamani@ucsd.edu

Abstract

Neuronal energy consumption is vital for information processing and memory formation in dendritic spines. The brain consists of just 2% of the human body's mass, but consumes almost 20% of the body's energy budget. Most of this energy is attributed to active transport in ion signaling, with calcium being the canonical second messenger of neuronal transmission. Here, we develop a model of synaptic signaling resulting in the activation of two protein kinases critical in metabolic regulation and cell fate, AMP-Activated protein kinase (AMPK) and mammalian target of rapamycin (mTOR) and investigate the effect of glutamate stimulus frequency on their dynamics. Our model predicts that higher frequencies of glutamate stimulus perturb AMPK and mTOR oscillations at higher magnitudes. This dynamic difference in AMPK and mTOR activation trajectories potentially differentiates high frequency stimulus bursts from basal neuronal signaling leading to a downstream change in synaptic plasticity. Further, we also investigate the crosstalk between insulin receptor and calcium signaling on AMPK and mTOR activation and predict that the pathways demonstrate multistability dependent on strength of insulin signaling and metabolic consumption rate. Our predictions have implications for improving our understanding of neuronal metabolism, synaptic pruning, and synaptic plasticity.

Abbreviations

AMP - Adenosine Monophosphate

ADP - Adenosine Diphosphate

ATP - Adenosine Triphosphate

AMPK - AMP-activated protein kinase

mTORC1 - Mammalian Target of Rapamycin Complex 1

mTORC2 - Mammalian Target of Rapamycin Complex 2

AKT - Protein Kinase B

ULK1 - UNC-51 like autophagy activating kinase 1

AMPAR - α-amino-3-hydroxy-5-methyl-4-isoxazolepropionic acid receptor

NMDAR - N-methyl-D-aspartate receptor

SIRT1 - Sirtuin 1

GLUT1-4 - Glucose Transporter 1-4

IP_3 - Inositol 1,4,5-trisphosphate

IP_3R - IP_3 receptor

RyR - Ryanodine receptor

SERCA - sarcoplasmic/endoplasmic reticulum calcium ATPase

ER - Endoplasmic reticulum

PMCA - Plasma Membrane Calcium ATPase

NCX - Na^+/Ca^{2+} exchanger

mGluR - Metabotropic glutamate receptor

PKC - Protein kinase C

PIP2 - Phosphatidylinositol (4,5)-bisphosphate

LTP - Long-Term Potentiation

LTD - Long-Term Depression

CAMKK2 - Calcium-Calmodulin Kinase Kinase 2

LKB1 - Liver Kinase B1

PI3K - Phosphoinositide 3-kinase

Introduction

Calcium signal transduction in dendritic spines during neuronal signaling is closely linked to synaptic plasticity [1–5]. Synaptic plasticity is the structural and molecular modification of synapses resulting in sustained changes in synaptic signaling strength [2, 6, 7]. There are many potential mechanisms by which calcium signaling leads to long-term plasticity (LTP), the process by which synaptic connections are strengthened with high-frequency stimulus, but the relative contribution of these different mechanisms is unclear [8]. One such mechanism is metabolic plasticity, which is the adaptation of cellular energy production in response to metabolic stress associated with calcium

signaling [9–11] and is the focus of our current work. Electrical signaling, including the reversal of presynaptic and postsynaptic ion fluxes, accounts for a vast majority of ATP consumption in mammalian neuron signaling [12, 13]. During an action potential, energy consumption is estimated to transiently increase up to 130 percent over basal ATP flux with most of this energy attributed to ion signaling, actin and microtubule turnover, and lipid and protein translation [12–14]. Therefore, the coupling of metabolic plasticity with ion dynamics is necessary for dendritic spines due to a drastic increase in energy consumption during neuronal signaling [11]. In addition, there are a variety of energetically expensive processes in the dendritic spine that are necessary to induce long-term potentiation (LTP) including actin remodeling, protein translation, endocytosis, and exocytosis [14]. The frequency of neurotransmitter signaling (Figure 1a) is believed to be critical in the induction of LTP in dendritic spines and also increases the consumption of cellular energy due to the increased rate of active transport of ions to restore resting potentials [13].

The two primary means of energy production within neurons are glycolysis and oxidative phosphorylation in the mitochondria [15, 16]. Glycolysis, the metabolism of glucose in the cytosol, is often upregulated during neuronal stimulus through increased import of glucose from extracellular space and protein kinase-dependent activation of enzymes. [17, 18]. Mitochondrial oxidative phosphorylation produces a large portion of cellular energy that supports increased energy demand. However, oxidative phosphorylation requires pyruvate and oxygen consumption to generate ATP in the mitochondrial matrix through mitochondrial metabolism of pyruvate driving the electron transport chain. In actively signaling neurons, mitochondria are observed to form spatially stable pools near the base of dendritic spine, suggesting that they can cater to the increased ATP demand by localizing ATP production proximal to the dendritic spine [19]. In conjunction, it has been observed that calcium influx from extracellular space impacts the mitochondrial membrane potential, resulting in higher ATP generation [20]. This provides a route for calcium, the main second messenger system in signaling, to interact directly with the energy production in a frequency-dependent manner. The thermodynamic constraints of ATP production in the mitochondria are explored in [21].

Calcium influx (Figure 1b) has been shown to indirectly modulate neuronal glycolysis and mitochondrial metabolism via enzymatic activation (CAMKII [22]), but the means by which neurons regulate the energy production local to the dendritic spine remains unexplored [20]. A possible avenue for feedback between neuronal energy consumption and metabolic production is through cellular energy sensors and kinases. Adenine monophosphate-activated Protein Kinase (AMPK) is a candidate molecule for the coupling between calcium dynamics and cellular metabolism due to its unique function as the cellular energy stress sensor [20, 23]. The γ subunit of this heterotrimeric protein is able to adapt to changing ratios of AMP and ATP, exposing a phosphorylation site and enabling kinase functionality [24]. Upstream regulators of AMPK include CAMKK2, LKB1, AKT, mTOR, and PI3K, which may activate or inhibit AMPK activation in neurons [22, 25, 26]. The downstream targets of AMPK include phosphofructokinase (PFK), mitochondrial biogenesis, and inhibition of energy consuming pathways like lipid synthesis and gluconeogenesis. Calcium-Calmodulin activated Kinase Kinase 2 (CaMKK2) enables direct feedback from the calcium signaling

pathway to AMPK. Indirectly, calcium creates an energy imbalance because of increased energy demand by ion channels and activates AMPK [11, 22, 23, 27]. AMPK activated by either of these pathways leads to feedback to dynamically enhance energy production. AMPK has been shown to increase the import of glucose into neurons by promoting trafficking of glucose import receptors GLUT3 to the plasma membrane [28]. Furthermore, AMPK upregulates glycolysis by modulating PFK activity during energy stress in cardiac cells as well as mitochondrial morphology in neuronal axons [29, 30].

One critical downstream target of AMPK is mammalian target of rapamycin (mTOR); selected interactions are shown in Figure 1c. mTOR is a well-conserved protein across mammalian cell types, but occupies a unique niche in neurons. While classically mTOR forms a protein complex that regulates protein translation and mitophagy [31], mTOR has also been shown to be critical in synapse formation [11, 31–33]. In presynaptic boutons, mTOR forms a complex with Rictor, mTORC2, which is necessary for bouton formation [31]. In postsynaptic dendritic spines, mTOR forms a complex with Raptor, mTORC1 [11]. mTORC1 has been shown to influence the translation and transport of α -Amino-3-hydroxy-5-methyl-4-isoxazolepropionic acid (AMPA) receptors and scaffolding proteins needed for the clustering of AMPAR, a critical step in synaptic plasticity [34]. Abolishment of mTOR activity in both presynaptic and postsynaptic cells has been performed in live neurons and shows a decrease in the number of spines and plastic ability [32, 34]. The exact mechanisms by which the calcium-AMPK-mTOR signaling axis is regulated in neurons are yet to be explored. In particular, exploration is needed to bridge the activity of calcium signaling, which typically occurs on the timescale of milliseconds, to the function of protein kinases (AMPK, mTOR, AKT), which can occur on the timescale of hours to days. AMPK and mTOR are also both downstream targets of the insulin receptor substrate (IRS) signaling cascade, which can bridge the intracellular response to a systems level change in insulin. A multi-timescale model that represents these different systems can shed light into the crosstalk between these two pathways.

In this work, we use computational modeling to explore how the calcium-AMPK-mTOR signaling axis could couple energy states and mTOR activity. Computational modeling has vastly contributed to our understanding of neuronal signaling and synaptic plasticity [1–4, 35–37]. However, very few of these models feature the importance of metabolic feedback mechanisms known to be critical in synaptic formation and activity. We built our model based on prior models in the literature, utilizing a calcium signaling model that incorporates the effect of endoplasmic reticulum (ER) and mitochondria on calcium signaling and mitochondrial ATP production [38]. We complement this calcium model with a model linking cellular energy state via adenine nucleotide balance with AMPK activation [39]. Finally, we explore the AMPK and mTOR crosstalk, which is integrated with insulin receptor substrate, and incorporate that within our calcium and metabolism model [26].

Our model predicts that a wide range of stability behavior is a possible outcome depending on glutamate stimulus, neuronal energy consumption, and the behavior of downstream components of the insulin signaling pathway. The

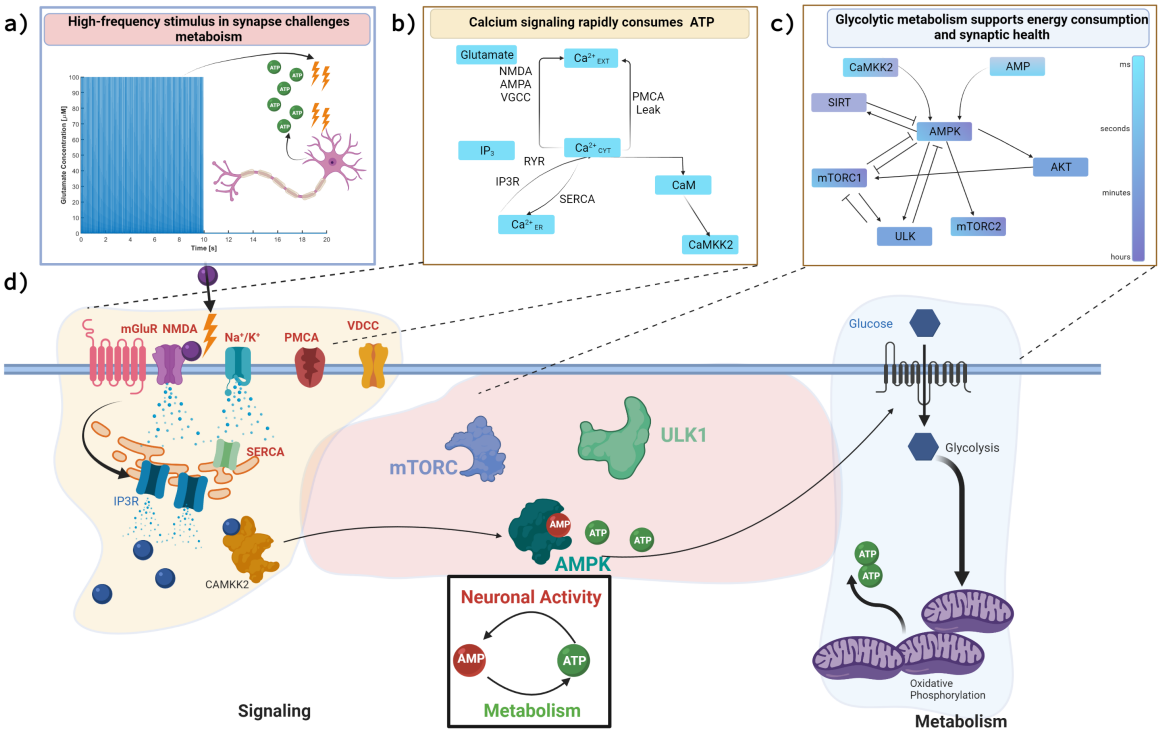

Figure 1: **Synaptic signaling consumes energy to transduce neuronal signals and support neuronal function.** During high-frequency synaptic signaling, represented with glutamate stimulus in **a)**, proportionally larger quantities of ATP are consumed and allocated to restoring resting potential of ions, like those shown for calcium illustrated in **b)**. At high frequencies, this may challenge the energy production capacity of neurons, which utilize glycolysis and oxidative phosphorylation to convert glucose to pyruvate and then produce ATP in mitochondria. The cellular energy state, quantified by the AMP/ATP ratio, promotes the phosphorylation of AMPK. AMPK is a kinase which promotes the production of cellular ATP, but also has an intricate feedback loop with mTORC1 and mTORC2, which have implications in protein translation and synaptic plasticity. In this work, we develop and analyze a computational model to study the interactions of these pathways in response to a synaptic stimulus across several time spans.

multistability of this system implies that the crosstalk between extracellular signals (Figure 1d), such as gluatamate and insulin, culminate in changes to internal metabolic systems such as AMPK and mTOR activation rates. Further exploration of the crosstalk between pathways may elucidate the relation between neuronal metabolism and signal processing in dendrites.

Methods

Model Description

All reactions used in our model are listed in Tables 1 to 3 and the system of differential equations for the glutamate receptor model is listed in Table 3. Here, we describe the various modules and the original sources for the reactions, where applicable. The system is composed of models representing AMPK and mTOR activation (Table 1), calcium dynamics (Table 2), and receptor dynamics NMDAR and AMPAR (Table 3).

Calcium dynamics

Intracellular calcium is a critical cellular second messenger that is closely linked to the induction of synaptic plasticity [40]. In this model, we source reactions established in legacy literature models of neuronal calcium [1–3, 36, 41]. Calcium influx is initiated by glutamate binding to receptors on the PSD described in receptor models. Calcium release from the endoplasmic reticulum (ER) is triggered through binding of IP3 to IP3R on the ER membrane, as well as calcium-induced calcium release by ryanodine receptors (RyR) [42]. These species are modeled as concentrations in compartments and described in the equations listed below:

$$\frac{d[Ca_C^{2+}]}{dt} = J_{RYR} + J_{IP3} - J_{SERCA} + J_{PM} + J_{ER,Leak} - J_{Buff} \tag{1}$$

$$\frac{d[Ca_{ER}^{2+}]}{dt} = -J_{RYR} - J_{IP3} + J_{SERCA} - J_{ER,Leak} - J_{ER,Buff} \tag{2}$$

Here, Ca_C^{2+} represents the calcium concentration in the cytosol and Ca_{ER}^{2+} represents the ER calcium concentration. Flux components of these differential equations are represented by Ryanodine (J_{RYR}), IP3 Receptor (J_{IP3}), SERCA pump (J_{SERCA}), plasma membrane calcium-atpase (J_{PM}), ER calcium leak ($J_{ER,leak}$), and buffering terms for the cytosol (J_{Buff}) and ER ($J_{ER,Buff}$) and are fully described in Table 2.

ATP Production and Consumption

ATP is rapidly consumed during synaptic activation due to the export of ions as well as many housekeeping reactions involved in synaptic plasticity [13, 14, 19, 43]. ATP is generated by glycolysis and oxidative phosphorylation. Glycolysis is a well-studied pathway in which cells metabolize glucose into pyruvate to generate ATP [16]. Computational models of glycolytic activity in neurons have provided predictions for neurodegeneration, pathology, and

development [44–46]. Pyruvate, the end product of glycolysis, is oxidized in mitochondria; in our model, oxidative phosphorylation is a function of mitochondrial potential computed by fluxes of the electron transport chain, as described by Beard [47]. In contrast, ATP is hydrolyzed to ADP to provide energy for many reactions in the cell. In our model, both ATP production and consumption are modeled as mass action kinetics based upon values from the literature [47]. However, the rates of energy consumption are dependent on synaptic signaling [12, 13]. In this model, we assume that the active synaptic energy consumption is correlated with the activity of active transporters, for example, SERCA and PMCA. In addition to active energy consumption from synapses, global energy consumption through maintenance and housekeeping reactions add up to the overall energy consumption rate predicted by the model. ATP, ADP and AMP are modeled in the cytosol as described in equations listed below:

$$\frac{d[ATP_C]}{dt} = J_{Glyc} + J_{OP} - J_{AK} - J_{CK} - 2J_{ATPCA} + J_{AMPK} \tag{3}$$

$$\frac{d[ADP_C]}{dt} = -J_{Glyc} - J_{OP} + 2J_{AK} + J_{CK} + 2J_{ATPCA} \tag{4}$$

$$\frac{d[AMP_C]}{dt} = -J_{AK} - J_{AMPK}, \tag{5}$$

where ATP, ADP, and AMP are nucleotide concentrations over time. The fluxes modeled in these equations include: Glycolysis (J_{Glyc}), Oxidative Phosphorylation (J_{OP}), Adenylate Kinase (J_{AK}), Creatine Kinase (J_{CK}), ATP consumption (J_{ATPCA}), and AMPK activation(J_{AMPK}) and are given in Table 1.

Receptor models

Glutamate release into the synapse from the presynaptic cell is modeled as a series of step functions during the stimulus duration, with stimulus frequencies ranging from 0.1 to 100 Hz (Figure 4a-c). The decay of glutamate within the synapse is based upon time constants from experiments by Clements [48]. NMDAR and AMPAR cascades are modeled as a multi-state receptor model with a prescribed voltage [49]. These equations are included in Tables 1 to 3 and parameters in Tables 4 to 7.

AMPK and mTOR Activation

AMPK and mTOR are coupled in an intricate feedback loop involving several other protein kinases. This system is directly downstream of insulin receptor signaling and is derived from Sadria [26] (shown in Figure 1). Sadria et al. developed an AMPK and mTOR signaling pathway for activity in cancer cells, parameterized from experimental data of mTOR activation in adipocytes of type 2 diabetes patients [50]. We have adapted the signaling network and differential equations for species including mTORC1, mTORC2, AKT, ULK1, SIRT1, IRS, and have integrated metabolic activation of AMPK by AMP/ATP ratio.

Mathematical Methods

The system of equations contains 60 species and 162 parameters. All equations were solved as a system of ordinary differential equations (ODE) using MATLAB's built-in stiff solver, ode15s [51]. These equations were integrated with a maximum timestep of 0.1 s, relative integration tolerance of 10^{-5}, using backward differentiation formulas with a maximum order of 4. Because each stimulus requires an instantaneous change in concentration and ODE solvers require a smooth, differentiable function, each stimulus was discretized to an individual ODE solution using the previous state as the subsequent initial condition. Before each simulation, the system was run to a steady state, approximately 10,000 seconds. The results of this initial simulation are included in Supplemental Figure 1 and all model files are included in the public repository (https://github.com/aleung15/AMPKmTOR2022).

Sensitivity Analysis

The dynamics of the model are dependent on both parameter values and initial conditions. The size and complexity of the system suggest nonlinear behavior such that changes in parameters for a single flux may lead to diverse response in the AMPK and mTOR concentrations. To elucidate the role of each parameter in the system output we perform local sensitivity analysis. In the local sensitivity analysis, a selection of parameters were varied 0.5 percent from their original value. These parameters were selected due to their relevance to AMPK and mTOR pathways as well as overall importance to pathway. The sensitivity index, indicated by the values on the color scale, was computed by the following formula:

$$S_I = \frac{dS/S}{dp/p}, \tag{6}$$

where S is the steady state concentration of AMPK or mTOR without changed parameter, dS is the simulation results with changed parameter, dp is the changed parameter value, and p is the original parameter value.

Results

Within a signaling synapse, the presynaptic neuron can send glutamate vesicles to a postsynaptic neuron from low frequencies (0.1 to 1 Hz) to high frequencies (10 to 100 Hz). Low frequency signaling is often associated with long term depression and synaptic pruning, while high frequency signaling is believed to induce long term potentiation (LTP), the mechanism behind neuronal learning [52, 53]. Each pulse of glutamate triggers a calcium influx into the neuron requiring a significant cellular energy cost in the form of ATP consumption for the restoration of resting ion potentials and various housekeeping processes (Figure 1b). As frequencies rise, there may be a critical point at which the ATP production from neuronal metabolism is overwhelmed by the energy demand. The metabolic plasticity, or the ability of the neuron to scale metabolic production to energetic demand, must be modeled alongside the closely

coupled calcium signaling cascade to understand how the neuron is able to induce synaptic plasticity during periods of extreme energy stress. In what follows, we investigate the crosstalk between synaptic signaling and metabolic plasticity.

Baseline system behavior and sensitivity analysis

We first analyzed the system behavior in the absence of stimulus to investigate how the coupled signaling networks behave. After a brief initialization period, we see a rapid equilibration of all species to an apparent steady state, shown in Supplemental Figure 1. Many trajectories on the short, millisecond to second, timescale equilibrate nearly instantaneously including calcium, receptors, AMP/ATP, and AMPK. However, several species, like mTORC1, mTORC2, and IP3, take much longer to reach an equilibrium, on the second to minute timescale. Since the initial conditions are misaligned with the equilibrium states determined by key parameters, there is a brief initialization period before equilibration. For example, as the AMP/ATP ratio is much higher than the equilibrium value, this induces AMPK activity which leads to mTOR and AKT activity. Nevertheless, the resulting transient behavior fades after 200 seconds as the dampened oscillations reduce to a fixed point, representing the system at rest. All subsequent simulations use this rest state as initial conditions before stimulus.

The steady state behavior of this system is dependent on both parameters and initial conditions. However, due to the complexity of the pathway and the large amount of species and parameters, not all parameters have an equivalent effect on the end result of the model. To quantify the effect of parameters on the critical model results, we compute the sensitivity index for a subset of parameters. The results of the local sensitivity analysis are shown in Figure 2a and Figure 2b for AMPK and mTORC2 respectively. Additionally, parameters that have a significant impact on the steady state of the system are bolded in Tables 4 to 7. Out of 162 total number of parameters, we show only the 40 most significant parameters. Other parameters have a much lower sensitivity index, less than 10% of the maximal sensitivity index. Parameters that appear to impact the steady state behavior of AMPK are related to the steady state of adenine nucleotides, oxidative phosphorylation, and feedback between mTORC1, mTORC2, AKT, and ULK1. AKT has an especially high sensitivity to mTORC1, which is one of its direct activators. Likewise mTORC1 has a higher sensitivity to IRS and AKT parameters. mTORC2 is sensitive to IRS activation; it appears to be relatively robust to changes in metabolic parameters. Having established the key parameters that the model is sensitive to, we next focus on the dynamic behavior of the coupled system in response to glutamate stimulus.

Low frequency neuronal stimulus reveals low amplitude transient behavior

After establishing the steady state behavior in the absence of stimulus (Supplemental Figure 1), we perturb the system with a 1 Hz glutamate pulse for 50 seconds. Glutamate stimulus induces a calcium influx (Figure 3a) into the cytosol through the glutamatergic receptors, which consequently induces ATP consumption related to ion transport,

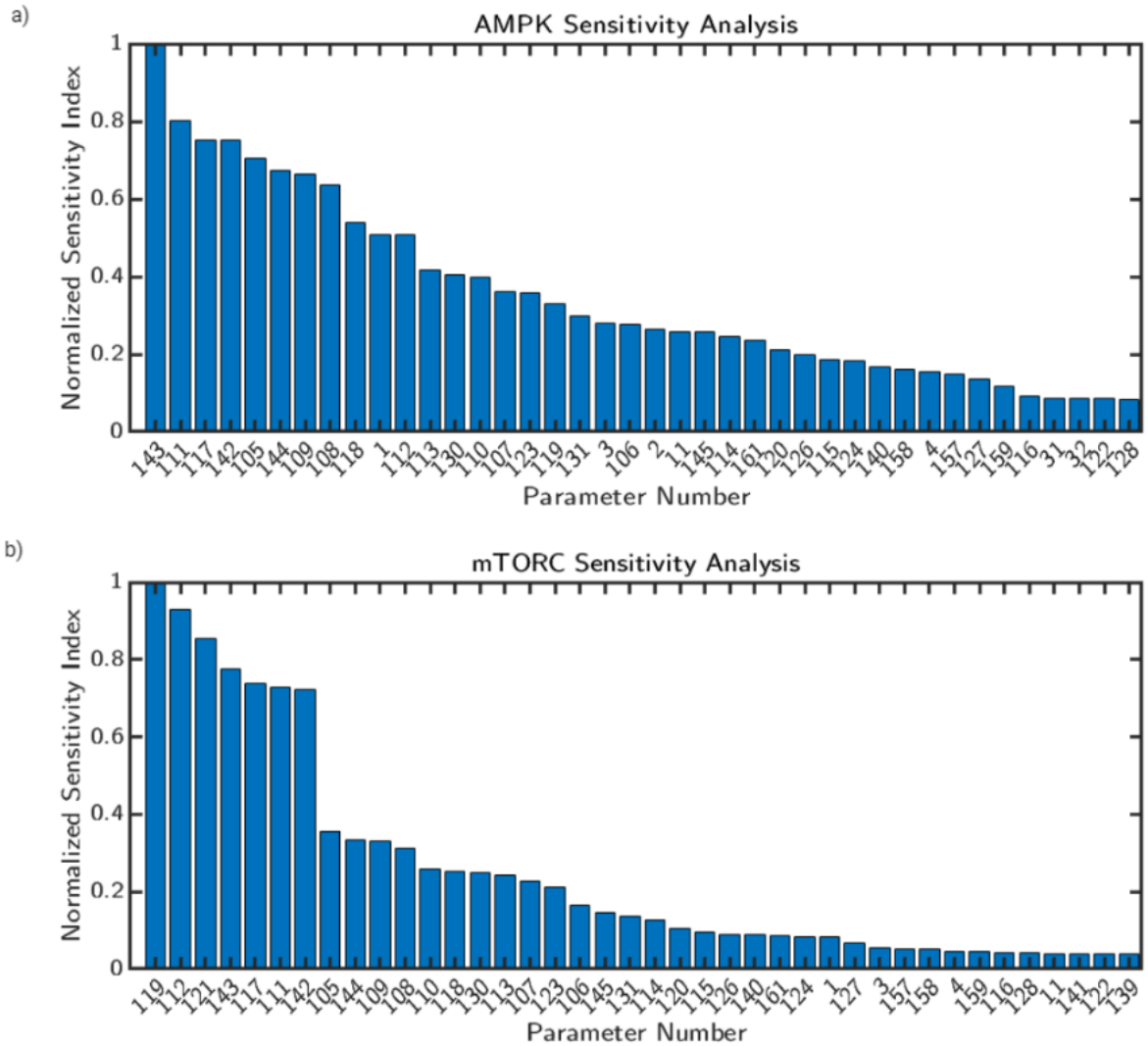

Figure 2: **Local sensitivity analysis reveal key parameters regulating system behavior.** The model describing AMPK and mTOR phosphorylation due to glutamate-stimulated calcium influx contains 162 parameters and 60 equations describing concentrations of molecules and receptor states in a well-mixed model. The parameter indices listed on the sensitivity analysis refer to their number listed in Tables 4 to 7 and the corresponding parameter vector in model files. **a)** Sorted sensitivity analysis for parameters influence on steady state concentrations of AMPK normalized to maximal sensitivity index. The top 40 parameters are shown. **b)** Sorted sensitivity analysis for parameters influence on steady state concentrations of mTORC2 normalized to maximal sensitivity index. The top 40 parameters are shown.

increases the AMP/ATP ratio (Figure 3b), and therefore AMPK activation. This AMPK activation (Figure 3c) then leads to an initial decrease of mTORC1 (Figure 3d), increase of mTORC2 (Figure 3e), and increase of ULK1 (Figure 3f).

Cytosolic calcium attains a peak calcium concentration of 4 μM and decays rapidly to the baseline concentration of 1.7 μM (Figure 3a). Due to the increased energy consumption associated with the calcium pumps in the model, AMP/ATP ratio increases during synaptic signaling to a peak value of 0.02 from its baseline value of 0.016 (Figure 3b). We note that both calcium and the AMP/ATP ratio (Figure 3b) match the frequency of the input glutamate. The oscillations of AMPK in the model induce subsequent oscillations of AMP/ATP ratio, as AMP and ATP are substrates in AMPK binding. pAMPK also shows a corresponding dynamic (Figure 3c); phosphorylated AMPK increases by 19% but returns to baseline activation analogous to the trajectory of cytosolic calcium concentration. The magnitude of change for critical terms like mTORC1, mTORC2, and ULK1 are fairly small during 1 Hz stimulus of glutamate. In response to this AMPK activation, mTORC1 deviates approximately 2.5% from its baseline value while mTORC2 deviates 5% over its unstimulated value (Figure 3d,e). Changes in ULK1 follow similar trajectories to mTORC2 with a 41% change in activation decaying shortly after stimulus ends back to unstimulated values (Figure 3f). We observed that while calcium, AMP/ATP ratio, and pAMPK responded with the same frequency as the glutamate stimulus, mTORC1, mTORC2, and ULK1 responded with a lower frequency, suggesting that this cascade filters out the high-frequency effects.

To further quantify the overall responses, we calculated the area under the curve (AUC) of the phosphorylated AMPK, mTORC1, and mTORC2 curves to show the changes in total signaling activity for each term (Figure 3g) [54]. We normalize this AUC to unstimulated values to obtain a ratio of stimulated AUC over baseline AUC to quantify the magnitude of change in signaling. The period of oscillations of AMPK is slightly shorter than mTORC1 and mTORC2 (Figure 3h). AMPK has a 15% amplitude change during stimulus (Figure 3i), which results in a 4% increase in AUC. Both mTORC1 and mTORC2 have relatively low changes in amplitude and AUC at this level of stimulus, under a 1% change in AUC and 5% change in maximal amplitude(Figure 3g,i). From these calculations, we conclude that the energy state (AMP/ATP ratio and pAMPK) are instantaneously responsive to the change in calcium and therefore upstream glutamate stimulus, thus the amplitudes of the downstream readouts are more resistant to responses to this particular stimulus pattern. This filtering mechanism is also apparent in the temporal response as well.

Effect of glutamate stimulus frequency on AMPK/mTOR pathway

We next investigated the effect of glutamate stimulus frequency on the activation profiles of key model outputs. The glutamate input stimuli, shown in Figure 4a-c, was varied from 0.1 Hz to 100 Hz, reflective of the range of potential stimulus frequencies in a signaling neuron [53]. While in Figure 3, we show only minor changes in state and

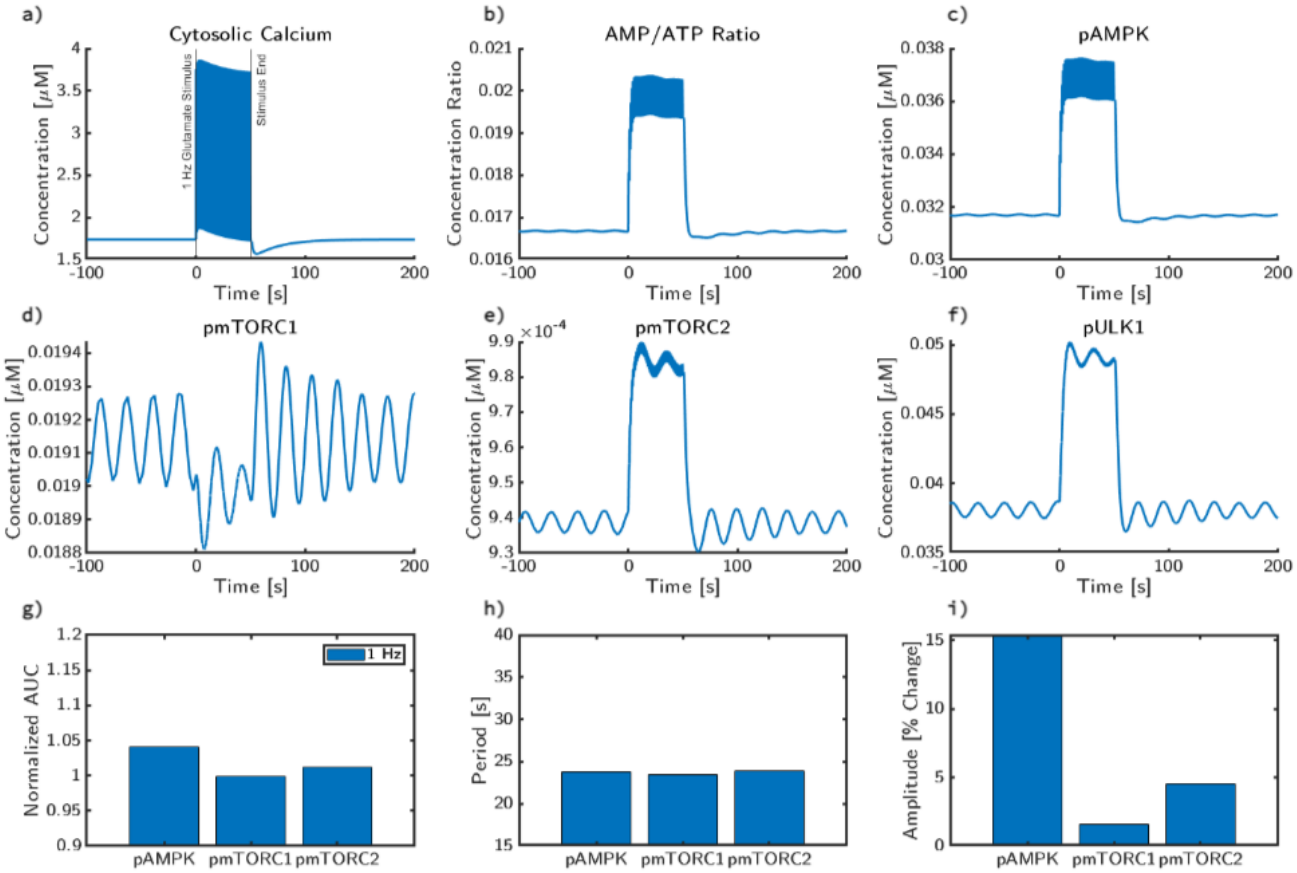

Figure 3: **Effect of a simple 1 Hz glutamate on AMPK/mTORC dynamics.** The stimulus to the system was a 1 Hz pulse train over 50 seconds. Before stimulus, the system was allowed to reach a steady state. During pulses of stimulus, 100 μM of glutamate is applied, which decays with a rate constant of 200 ms. After stimulus, the system was allowed to return to an apparent equilibrium with no additional glutamate input. Concentration trajectories for **a)** cytosolic calcium concentration, **b)** cytosolic AMP/ATP ratio, **c)** cytosolic phosphorylated AMPK concentration, **d)** phosphorylated mTORC1 concentration, **e)** phosphorylated mTORC2 concentration, **f)** phosphorylated ULK1 concentration are shown. To quantify the behavior of this system we compute **g)** the area under the curve (AUC) relative to the unstimulated system, **h)** the period between peaks, and **i)** the change in maximum amplitude for AMPK, mTORC1, and mTORC2.

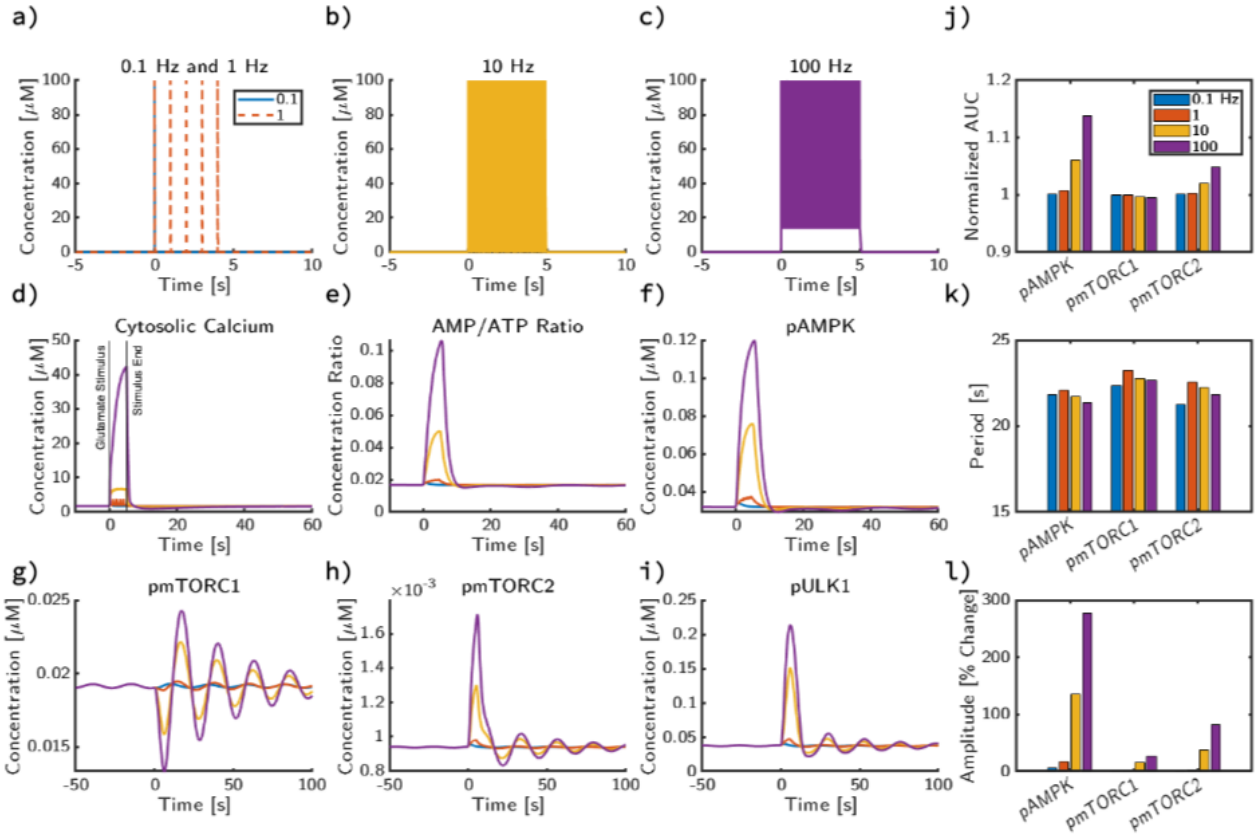

Figure 4: **mTOR oscillations are stimulus frequency dependent**. The system was stimulated with four different glutamate frequencies: **a)** 0.1 Hz (Blue), 1 Hz (Orange), **b)** 10 Hz (Yellow), **c)** 100 Hz (Purple). After stimulus, simulations return to an apparent equilibrium with no additional glutamate input. Trajectories are shown for **d)** cytosolic calcium concentration, **e)** cytosolic AMP/ATP ratio, **f)** cytosolic phosphorylated AMPK concentration, **g)** phosphorylated mTORC1 concentration, **h)** phosphorylated mTORC2 concentration, **i)** phosphorylated ULK1 concentration. Quantitative metrics for AMPK, mTORC1, and mTORC2 in response to pulse trains of glutamate stimulus are also shown. **j)** Area under the curve (AUC) relative to the system without stimulus applied over the same integration window (100 seconds). **k)** Average period of oscillations. **l)** Amplitude change quantified as percent change from basal oscillations.

overall signaling effect, as stimulus frequency increases, cytosolic calcium concentration and ATP consumption also increase (Figure 4d-e). The change in calcium concentration is dependent on the frequency of glutamate stimulus (Figure 4d); as stimulus frequency increases, calcium amplitude increases and the higher frequencies are filtered out. There is a corresponding ATP consumption that leads to an increase in the AMP/ATP ratio (Figure 4e), which leads to AMPK activation (Figure 4f). Without stimulus, mTORC1 (Figure 4g) and mTORC2 (Figure 4h) oscillate around an average value of 0.019 μM and 0.0009 μM. When AMPK is activated, we observed a large initial perturbation from the baseline oscillatory pattern that results in damped oscillations that eventually return to equilibrium concentrations. The maximum amplitude of the deviations from equilibrium of mTORC1, mTORC2, and ULK1 (Figure 4g-i) are dependent on the amplitude of AMPK activation, and therefore glutamate stimulus frequency (Figure 4l).

The AUC over 100 seconds (Figure 4j) represents the total amount of a species within the system during response to signaling events. Since the concentrations of each species can be orders of magnitude apart, we normalized each AUC to the baseline activity profiles to obtain a relative AUC value. In Figure 4j, we observed a frequency-dependent increase in the AUC of AMPK and mTORC1 and a decrease of mTORC2's AUC. At low frequency conditions (0.1 and 1 Hz), the AUC of all species does not change significantly. As frequency increases, AMPK activation increases proportionally to the highest stimulus frequency, where AMPK's AUC increases by 14 % after exposure to 100 Hz stimulus for 5 seconds. While the overall magnitude of change for mTORC1's AUC is lower in comparison to pAMPK and mTORC2 for all frequencies, there is a slight decrease as frequency increases. Inversely, as AMPK phosphorylation increases, mTORC2's AUC also increases. Next, in Figure 4k and Figure 4l, we characterized the oscillatory behavior of the trajectories through its period and amplitude. For all three species, the 1 Hz stimulus had a longer average period as compared to 0.1 Hz stimulus and as frequency increases, the period of AMPK, mTORC1, mTORC2, and ULK decreases. We also observed that the amplitude change for AMPK, mTORC1, and mTORC2 increases with increasing frequency.

Increasing basal energy consumption increases AMPK activation

While calcium and other ion transport are known to be primary drivers of energy consumption in neurons, there are additional energy consuming processes that require ATP in the dendritic spine. For example, it is thought that actin, which is abundant in dendritic spines, is one of the main non-signaling ATP sinks through actin polymerization and remodeling [55]. Additionally, protein and lipid turnover in neurons can consume up to 25% of the total ATP consumed in brain tissue [14, 56].

To explore the interaction between the basal energy consumption rate and the glutamate stimulus on AMPK signaling, we designed a series of simulations using our model. In our model, energy consumption is simplified as a lumped parameter representing ATP hydrolysis in the cytosol, k_{hyd}. We varied this parameter to capture the effect of different energy consumption rates. We held our glutamate stimulus to 10 Hz because this stimulus approximates

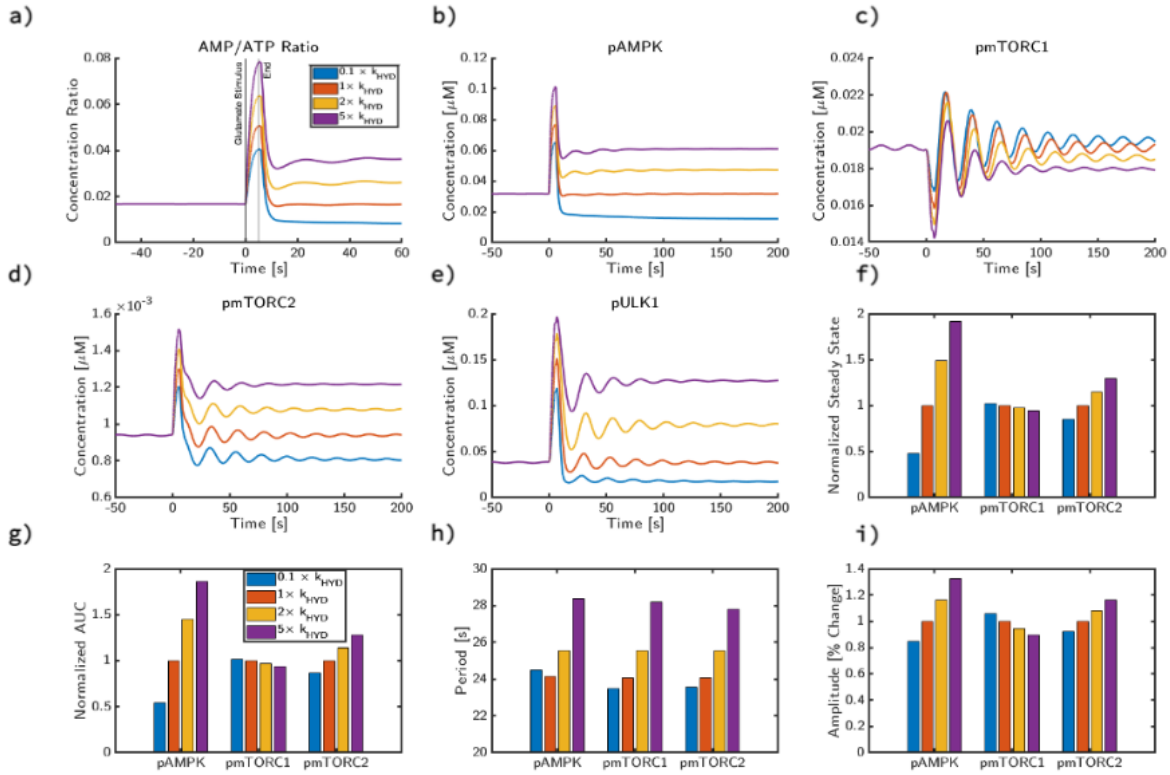

Figure 5: **Cellular metabolic rate influences steady state behavior of AMPK and mTOR independent of calcium**. We apply a 10 Hz glutamate stimulus for 5 seconds, however at t=0s, we also change the value of baseline energy consumption throughout the cell and plot concentration trajectories for **a)** AMP/ATP, **b)** active, phosphorylated AMPK, **c)** active, phosphorylated mTORC1, **d)** active, phosphorylated mTORC2, **e)** active, phosphorylated pULK1. Additionally, in **f)**, we compare the changes in steady state for pAMPK,mTORC1, and mTORC2 with respect to changes in hydrolysis rate. In **g)**, we then compare how this change impacts AUC, normalized to the AUC of simulation with the base value of the parameter. In **h)**, we plot the period and in **i)**, the relative magnitude of the first peak of AMPK, mTORC1, and mTORC2 as a result of energy consumption from glutamatergic stimulus.

the threshold of frequency necessary to trigger change in mTOR (Figure 4).

We found that varying k_{hyd} had a nonlinear effect of the AMP/ATP ratio (Figure 5a). There was no change in calcium dynamics since the calcium influx depends on the NMDAR fluxes, which are not dependent on hydrolysis rates. Compared to the baseline value, a 10-fold decrease in k_{hyd} decreases the AMP/ATP ratio by a small amount but a 5-fold increase in k_{hyd} increases AMP/ATP ratio dramatically. This nonlinearity in steady state is also observed in pAMPK (Figure 5b), where a nonlinear increase in pAMPK levels is seen for a 5-fold increase in the energy consumption rate. Interestingly, changing k_{hyd} actually changes the oscillation pattern for pmTORC1 (Figure 5c). Increase in the energy consumption rate translates the damped oscillations observed in pmTORC1 at lower energy consumption rates into a stable steady state, without any oscillations, at high energy consumption rates. This effect is also seen in the dynamics of pmTORC2 (Figure 5d) and pULK1 (Figure 5e) except that increasing basal energy consumption increases the level of pmTORC2 and pULK1. Further analysis of these variations reveals that the steady state depends on the basal energy consumption (Figure 5f).

Next, we characterize the effect of hydrolysis rates on the stability features of AMPK, mTORC1, and mTORC2 signaling by plotting the normalized AUC, period of oscillation, and percent amplitude (Figure 5g-i). For AMPK phosphorylation, there is an increase in AUC with increasing k_{hyd}. From the baseline value of k_{hyd}, reducing k_{hyd} to a tenth of its original value roughly produces an AUC of half. However, the increase of k_{hyd} to $5 \times k_{hyd}$ and $10 \times k_{hyd}$ only increases the relative AUC by 50% and 150%, respectively. For mTORC1, while the decrease in AUC with increasing k_{hyd} is apparent, the magnitude of decrease is not as high when compared to AMPK. This trend can qualitatively be observed in Figure 5c, as the variations of k_{hyd} from 0.1 to $2 \times k_{hyd}$ have roughly the same trajectories, but the variation to $5 \times k_{hyd}$ reduces the steady state substantially. For mTORC2, the AUC increase from 0.1 to $2 \times k_{hyd}$ is minor, however $5 \times k_{hyd}$ produces a 60% jump in AUC. The periodicity of AMPK peaks increases with both increasing and decreasing k_{hyd} from baseline value. However, mTORC1 and mTORC2 period both follow similar trends of increase relative to k_{hyd}. The amplitude change, defined relative to the equilibrium values of amplitudes in steady state oscillations, depends on the magnitude of k_{hyd} since, as shown in Figure 5f, the steady state is dependent on k_{hyd}. Therefore, for AMPK, as k_{hyd} increases, the percent change in amplitude decreases. For mTORC1, there is a competing effect – as k_{hyd} increases, the magnitude of deviation change increases, but the equilibrium values decrease. For mTORC2, as the steady state values increase with increasing k_{hyd} but the percent change of amplitude decreases. Thus, we found that the stability features of the AMPK/mTOR pathway depend on the basal rate of ATP hydrolysis – increasing ATP consumption allows the system to transition from an oscillatory state to a stable steady state.

Insulin signaling and metabolic signaling interact to govern stability features

Thus far, we have explored the impact of glutamate stimulus and energy consumption on AMPK and mTOR activation. We next investigated the role of the insulin response pathway and its crosstalk with the glutamate pathway. Insulin receptor signaling is a primary input in metabolism and influences the phosphorylation state of AMPK, mTORC1, and mTORC2. In the model originally developed by Sadria [26], the insulin receptor substrate (IRS) directly interacts with AMPK and mTORC2, resulting in regimes of oscillations dependent on the rate of IRS phosphorylation. Since we included this pathway in our model, we now explore the feedback between the IRS pathway and AMPK pathway through the energy consumption rate. In our model, the parameters controlling the IRS phosphorylation rate and energy consumption rate are, V_{IR} and k_{hyd}, respectively. Here, we investigated how V_{IR}, k_{hyd}, and glutamate stimulus impact the AMPK-mTOR pathway.

In Figure 6, we show how the stability of this system is dependent on the magnitude of k_{hyd} and V_{IR}. First, for hydrolysis (Figure 6a,b), we select two values of V_{IR} to hold constant (5.7366 mM/s yellow and 0.01 mM/s in purple) and vary the rates of k_{hyd} (1000 values between 1×10^{-4} to 1 mM/s). We simulate the system in the absence stimulus until the system reaches its equilibrium state for each parameter combination and compute the minima and maxima as a function of V_{IR}. We observed that for the lower value of V_{IR}, increasing k_{hyd} gives a single unique steady state for both mTORC1 and mTORC2 (Figure 6a, b). For higher values of V_{IR}, we found that the stability behavior has an oscillatory regime for low values of k_{hyd} and a single steady state for high values of k_{hyd}. Thus, the hydrolysis rate alone can alter the stability features of the coupled system. Next, to obtain the relation between stability and V_{IR} values, we select two values of k_{hyd} and vary with 60 values of V_{IR} (from 0.1 to 20 mM/s), shown in Figure 6c,d. In Figure 6c, we compute the minima and maxima as a function of V_{IR} to show the stability features for two values of k_{hyd}, 0.0001 (Blue) and 0.14 (Red) [mM/s]. For low and high values of V_{IR}, minima and maxima curves converge to a singular value. However, there is a range of V_{IR} values in which the curves diverge. In this range, we see oscillations similar to those seen in the equilibrium states of Figure 3c-f. Values of V_{IR} that result in oscillatory behavior are correlated with hydrolysis; as k_{hyd} increases, a smaller range of V_{IR} produces oscillations. Compared to a low value of k_{hyd} (blue, 0.0001 [mM/s]), a high value of k_{hyd} (red,0.14 [mM/s]) shows a significantly smaller range of values, as well as a much smaller range of oscillations. This same approach is taken with Figure 6d for mTORC2.

Finally, we varied both k_{hyd} and V_{IR} and plot the same curves as surface plots in 3D. For mTORC1 (Figure 6e), rising V_{IR} leads to an increase in the steady state. Furthermore, increasing k_{hyd} reduces the range of values that produce oscillatory behavior. Outside the oscillatory regime, mTORC1 has a monotonic relationship with V_{IR}. Within the parameter range studied, the steady state behavior of mTORC1 is strongly related to the magnitude of V_{IR}, while k_{hyd} has diminishing impact past the oscillatory envelope. For mTORC2 (Figure 6f), a similar regime of oscillations was found. However, for mTORC2, V_{IR} does not strongly affect the magnitude of mTORC2 at steady

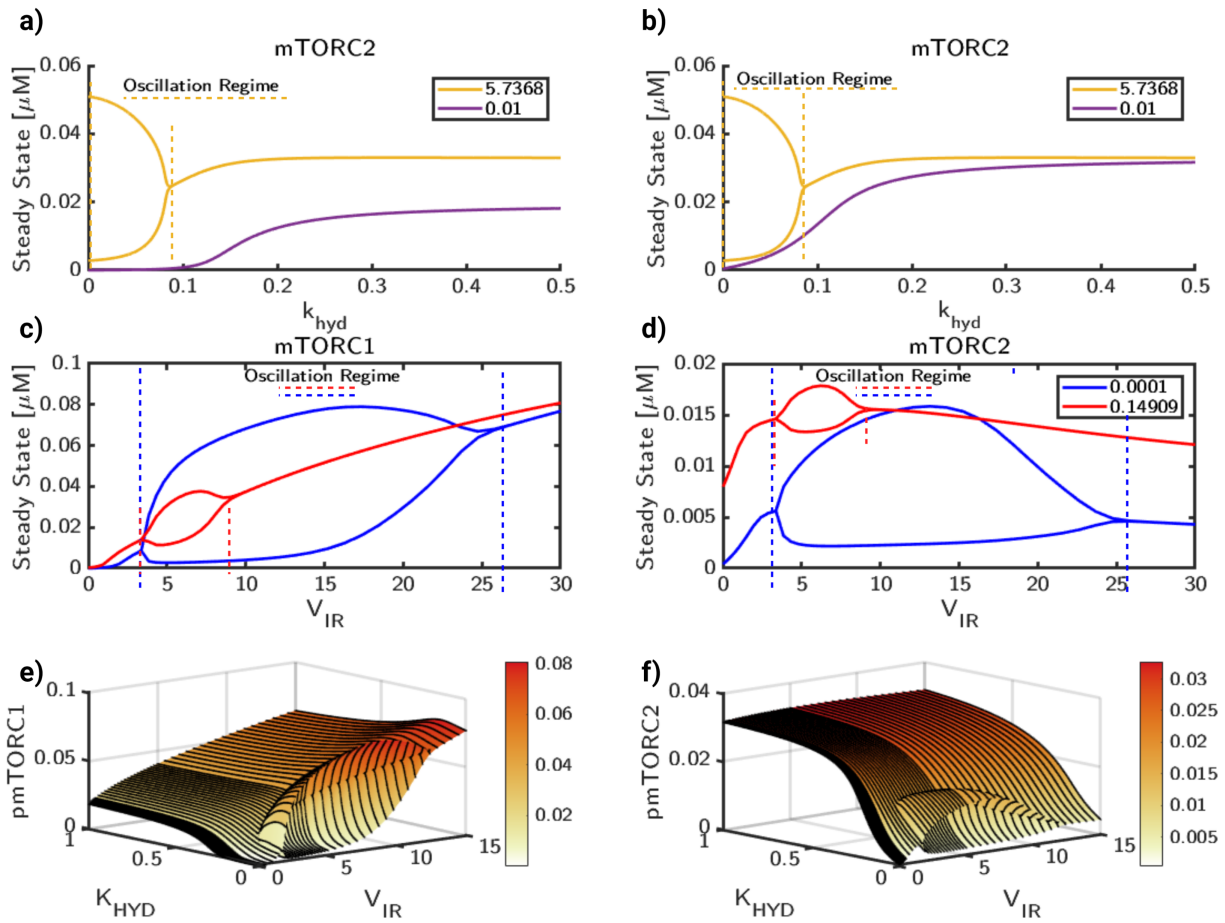

Figure 6: **Oscillatory regimes for mTOR activation are dependent on both metabolic activity and IRS** System displays multistability and oscillatory behavior dependent on both k_{hyd} and V_{IR} rates. We show the dependence of **a)** mTORC1 and **b)** mTORC2 stability on k_{hyd} by selecting two values of V_{IR}, 5.7366 [mM/s] (yellow) and 0.01 [mM/s] (purple). For each case, we simulate until an apparent steady state for a range of k_{hyd} and plot the curves of minima and maxima at equilibrium. In the oscillatory region, the minima and maxima diverge and show an oscillatory regime, denoted by yellow dashed line. Next, we hold k_{hyd} constant and vary V_{IR} to obtain the stability profiles for **c)** mTORC1 and **d)** mTORC2 dependent on V_{IR} For two values of k_{hyd}, 1×10^{-4} [mM/s] and 0.143 [mM/s] we simulate until an apparent steady state for a range of V_{IR}, then plot the curves of local minima and maxima at equilibrium for mTORC1 and mTORC2. For regions of monostability, outside of dashed lines, the curves of minima and maxima converge to the steady state. In oscillatory regimes, within the dashed lines, the local minima and maxima due to oscillations form an envelope. The size and shape of the envelope is dependent on both k_{hyd} and V_{IR}. Then, to characterise this relation in a 2D parameter space, we plot corresponding 3D surface plots for **e)** mTORC1 and **f)** mTORC2.

state. In contrast to mTORC1, in which V_{IR} was the primary controller of mTORC1 steady state, k_{hyd} results in a much stronger increase mTORC2 steady state for all values of V_{IR}.

Signaling frequency, ATP consumption, and insulin signaling modulate system response to energy stress

Thus far, we have investigated the impact of glutamate frequency alone (Figure 4) and the bifurcation behavior of the metabolic pathways in Figure 6. We next investigated how glutamate stimulus frequency, IRS, and hydrolysis rate combine to influence the energy state of the system. First, in Figure 7, we observe the trends associated with changes in V_{IR} and k_{hyd} under a 10 Hz stimulus pulse for 5 seconds. Trajectories for pAMPK, mTORC1, and mTORC2 are shown in Figure 7a-c. In these trajectories, the line color refers to the magnitude of V_{IR} while the line markers represent the k_{hyd} magnitude. Qualitatively, increases in k_{hyd} correspond to small concentration shifts of the trajectories predicted by V_{IR}. Concentration trajectories for AMPK are shown in Figure 7a. We observed that for all the trajectories, the peak activity corresponds with the time of the stimulus. However, the size of this peak is dependent on the magnitude of both parameters, but shows a stronger dependence on k_{hyd}. For mTORC1 (Figure 7b), we see a much stronger dependence on V_{IR} for the magnitude and behavior of mTORC1 trajectories. Interestingly, while increase in k_{hyd} leads to shifts in the baseline for higher V_{IR} values, in the range of values that show oscillations, k_{hyd} appears to have minor shifts in the time domain. Furthermore, oscillations are abrogated by higher values of k_{hyd}, which is consistent with the higher non-oscillatory regime of mTORC1 found in Figure 6e. For mTORC2 (Figure 7c), there are minimal changes associated with small changes in parameters, but the largest variation tested with k_{hyd} and V_{IR} (both 10 $\times$ their normal value) results in a change in overall baseline.

The relative AUC of the trajectories in Figure 7a-c are then quantified and summarized in Figure 7d-f. Since the curves can be vastly different in magnitude, for ease of comparability all AUC's are ratios of the AUC of an un-stimulated system under the same integration duration and then normalized to the maximum AUC for the selected trajectories. For AMPK (Figure 7d), increasing V_{IR} and k_{hyd} both lead to increases in AUC, with larger increases correlated to higher magnitudes of k_{hyd}. For mTORC1 (Figure 7e), increasing V_{IR} increases mTORC1 AUC, but increasing k_{hyd} leads to a decrease in mTORC1 AUC. Finally, for mTORC2 (Figure 7f), the magnitudes for most of the trajectories are similar. However, the trend follows that increasing both V_{IR} and k_{hyd} also increases the mTORC2 AUC. The largest magnitude increase of mTORC2 activation comes from when both k_{hyd} and V_{IR} are highest.

We next analyzed the interaction of the insulin substrate strength, V_{IR}, with the glutamate stimulus frequency (Figure 8). V_{IR} does not have a major influence on AMPK activity (Figure 8a), which is primarily influenced by glutamate frequency. But, as shown previously in Figure 4, higher frequencies above 10 Hz induce large transient pulses of AMPK activity. mTORC1 (Figure 8b) is significantly more sensitive to the magnitude of V_{IR} than to the input frequency, although the steady state behavior depends on the frequency. Increasing the frequency of stimulus can lead to higher amplitudes of dampened oscillations, but if the system is outside of the oscillatory regime it returns to

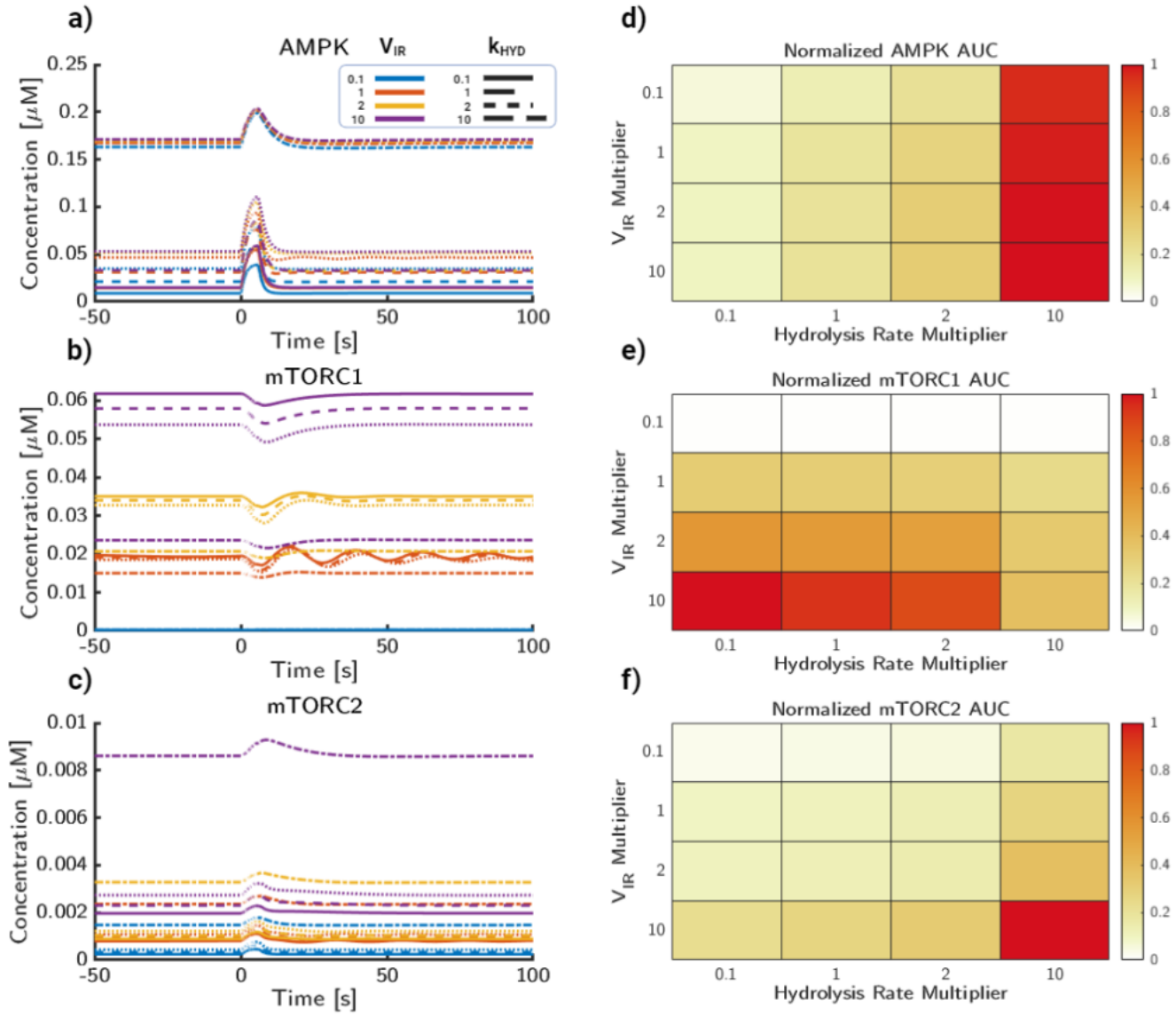

Figure 7: **Insulin and cellular metabolism govern phosphorylation rates of AMPK, mTORC1, and mTORC2.** **a)** AMPK phosphorylation concentration trajectories for a range of values for insulin receptor activity,V_{IR}, and ATP consumption rates, k_{hyd}. **b)** mTORC1 phosphorylation concentration trajectories for a range of values for insulin receptor activity,V_{IR}, and ATP consumption rates, k_{hyd}. **c)** mTORC2 phosphorylation concentration trajectories for a range of values for insulin receptor activity,V_{IR}, and ATP consumption rates, k_{hyd}. **d)** AMPK normalized AUC of system without stimulus over the same period of integration. **e)** mTORC1 normalized AUC of system without stimulus over the same period of integration. **f)** mTORC2 AUC of system without stimulus over the same period of integration.

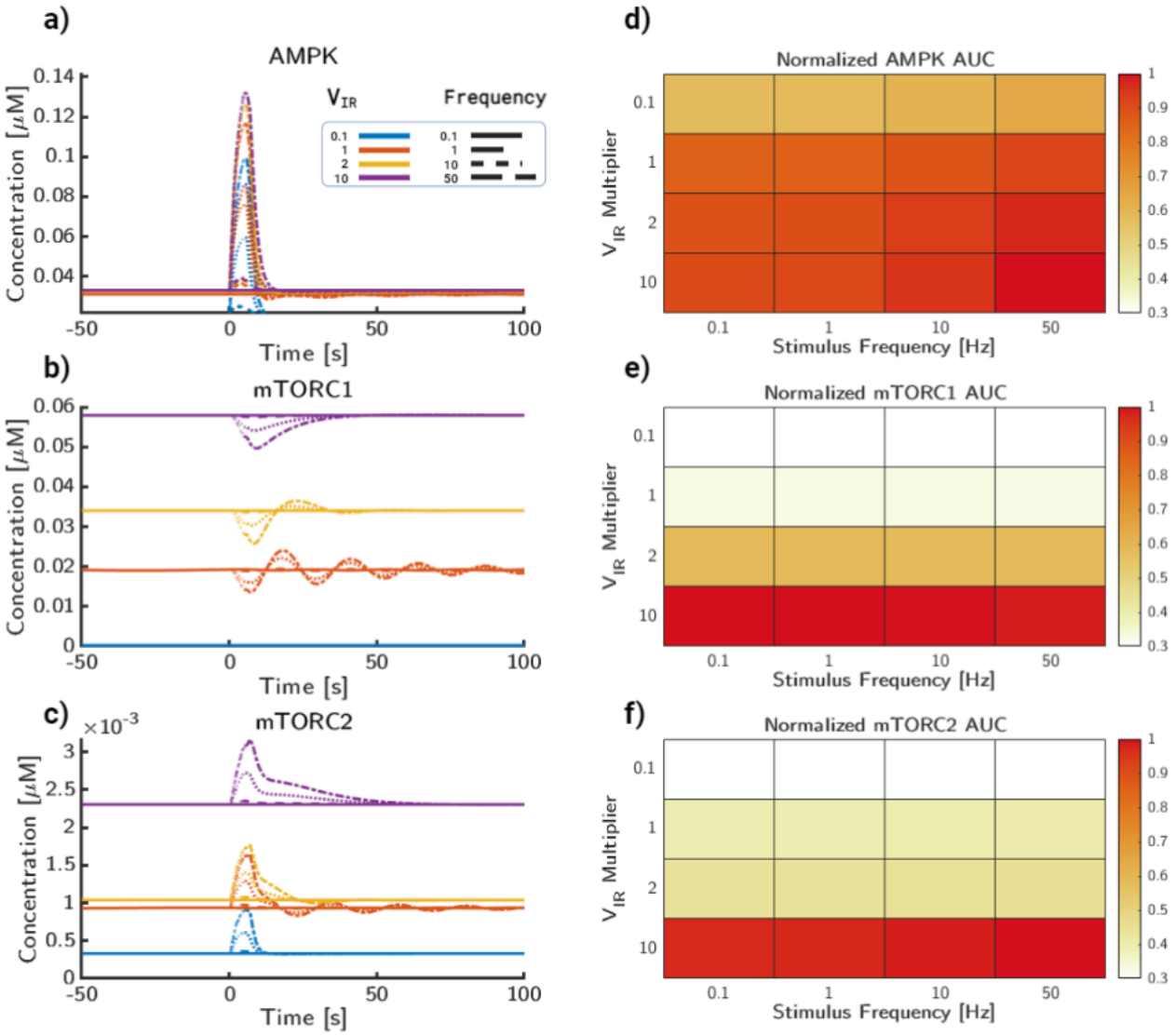

Figure 8: **Insulin signaling and glutamate frequency influence dynamic behavior of AMPK and mTOR phosphorylation. a)** AMPK phosphorylation concentration trajectories for a range of values for insulin receptor activity and glutamate stimulus frequency. **b)** mTORC1 phosphorylation concentration trajectories for a range of values for insulin receptor activity and glutamate stimulus frequency. **c)** mTORC2 phosphorylation concentration trajectories for a range of values for insulin receptor activity and glutamate stimulus frequency. **d)** AUC for AMPK normalized to the baseline AUC. **e)** AUC for mTORC2 normalized to the baseline AUC. **f)** AUC for mTORC2 normalized to the baseline AUC.

a steady state. This is the case for the high-frequency cases of both 0.1 and 10 $\times$ V_{IR}, in which no dampened oscillations are shown after approximately 50 seconds. A similar case is observed with mTORC2 (Figure 8c), in which both V_{IR} and stimulus frequency impact the initial peak height. However, particularly at cases of high frequency and also high V_{IR} magnitude, there appears to instead be a delayed return to steady state. Oscillations are still observed in 1 and 2 $\times$ V_{IR} cases, but are less pronounced.

The relative AUC (Figure 8d-f) is quantified in the same process as Figure 7. For AMPK (Figure 8d), the relative magnitudes of AUC are fairly similar across all cases, with the exception of low V_{IR} shifting the baseline of AMPK down in the 0.1 $\times$ V_{IR} row. The highest magnitude of AUC for AMPK comes from both high stimulus frequency as well as high V_{IR} magnitude. For mTORC1 (Figure 8e), while there is a clear increase in AUC while V_{IR} magnitude increases, any differences due to frequency are minimal. This implies that the stimulus frequency does not impact the overall signaling capacity of mTORC1, but may impact the dynamics of signaling on short timescales. Likewise, mTORC2 (Figure 8f) similarly shows a dependence on V_{IR} magnitude for overall mTORC2 AUC. However, as frequency increases, the AUC increases.

Finally, we analyze interactions between signaling frequency and ATP consumption rate (Figure 9). As before, stimulus frequency appears to be the largest driver of transient stimulus for AMPK (Figure 9a). As frequency increases, the time AMPK returns back to equilibrium is delayed, especially for higher magnitudes of k_{hyd}. The rate of k_{hyd} can also significantly raise the baseline values of AMPK activation, which is consistent with its model function and AMPK's activation conditions as the AMP/ATP ratio increases with higher k_{hyd}. For mTORC1 (Figure 9b), k_{hyd} does not have a strong impact to the activation rates of k_{hyd}, except at very high rates of k_{hyd}. The stimulus frequency, however, has a strong correlation with increased amplitude of mTOR. For mTORC2 (Figure 9c), frequency again shows an increased transient amplitude increase, but not a significant change to the overall trajectories. Likewise, k_{hyd} only appears to significantly change the state of mTORC2 when it is very high, 10 $\times$ the resting rate of ATP consumption.

The relative AUC (Figure 9d-f) is quantified in the same process as Figure 7. For AMPK (Figure 9d), the relative AMPK AUC shows a strong dependence on k_{hyd}, but also a minor increase due to frequency. For mTORC1 (Figure 9e), frequency changes appear to affect the dynamics of the system, but not necessarily the AUC. While the initial peak heights increase, this does not appear to impact the overall signaling capacity of the system. However, this may lead to differences in short timescale activation profiles of mTOR and its downstream targets. For mTORC2 (Figure 9f), the AUC shows an overall increase with hydrolysis rate. It also displays a minor increase due to signaling frequency, particularly at higher hydrolysis rates. In summary, we shown that crosstalk between glutamate frequency and metabolic signaling plays an important role in protein kinase activity, which has implications on cell fate and neuronal function.

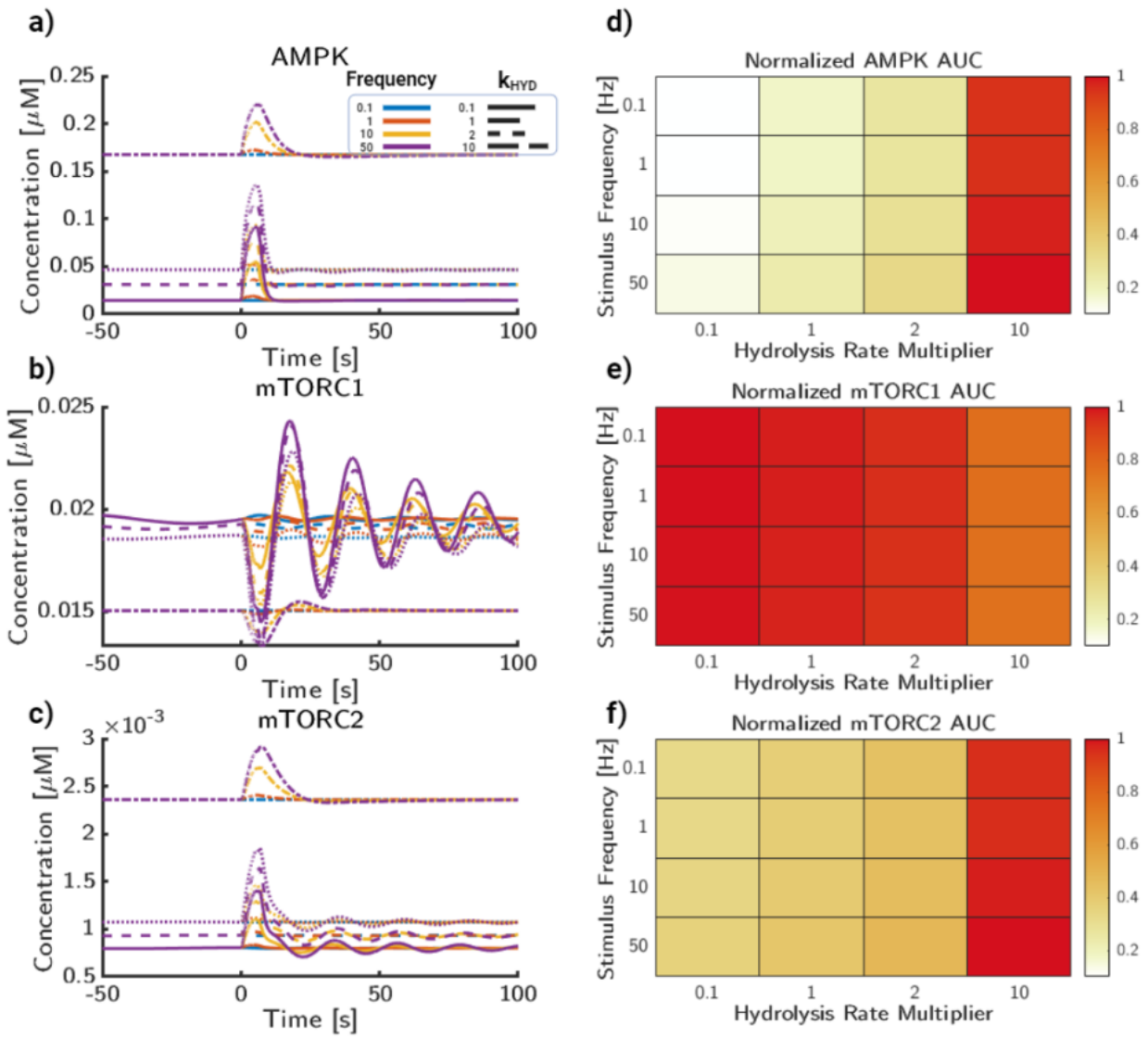

Figure 9: **Glutamate frequency and metabolic stress lead to increases in AMPK and mTOR deviations. a)** AMPK phosphorylation trajectories for a range of values for glutamate frequency and ATP consumption rates, k_{hyd}. **b)** mTORC1 phosphorylation trajectories for a range of values for glutamate stimulus frequency and ATP consumption rates, k_{hyd}. **c)** mTORC2 phosphorylation trajectories for a range of values for glutamate stimulus frequency and ATP consumption rates, k_{hyd}. **d)** AUC for AMPK normalized to maximal AUC value. **e)** AUC for mTORC1 normalized to maximal AUC value. **f)** AUC for mTORC2normalized to maximal AUC value.

Discussion

In this study, we have investigated the crosstalk between calcium influx in dendritic spines and mTOR and AMPK activation bridging multiple timescales of signaling in the context of dendritic spines. The pathways explored here

have significant implications for synaptic plasticity. Our main predictions focus on the possible multistability regimes in the system as a function of crosstalk between signaling and metabolic pathways. We find that the model exhibits a parameter-dependent oscillatory behavior, which can enable neurons to tune the cellular response to stimulus-based upon energy consumption, extracellular factors like insulin signaling, and signaling frequency.

It is believed that synaptic plasticity is triggered mainly through high-frequency signaling [52]. While the exact mechanisms contributing to synaptic plasticity are unknown, various works have shown that it is dependent on subcellular structure, calcium signaling, metabolics, and many other intermediary proteins including mTOR [4, 53, 57, 58]. Additionally, the mechanisms contributing to synaptic pruning and loss of dendritic spine density are unknown. In such complex processes, mathematical modeling may be able to contribute strongly to our understanding of crosstalk between signaling, metabolism, and synaptic plasticity.

We predict that the cellular response to energy consumption and external cellular signaling are frequency dependent and produce ranges of cellular stability behavior. Specifically, the range of oscillations between low and high energy states can contribute to distinct signaling mechanisms. Furthermore, the oscillatory state may serve as a buffer range between random or noisy neuronal signals and high-frequency signals that invoke LTP in synapses. While it is known that AMPK hyperactivation can contribute to synaptic pruning [59], these oscillations allow the system to reach higher rates of AMPK activation without raising the relative AUC. In this sense, oscillations controlled by the insulin system may regulate the levels of energetic stress that a neuron can withstand before triggering autophagy pathways. Pharmacological experiments for AMPK and mTOR activators in dendritic spine could show a change in sensitivity to glutamatergic stimulus and subsequently affect LTP and LTD.

Models of synaptic plasticity can be generalized to phenomenological models (including rate based models and spike timing based models) and biophysical models which generally focus on calcium signaling and downstream signal transduction via CAMKII [7,60,61]. However, looking forward, models of synaptic plasticity can incorporate crosstalk effects of insulin on downstream components in biophysical models of synaptic plasticity. Insulin signaling has been shown to regulate neuroplasticity in both developing and adult brains [62]. While this can be explained by reports that insulin can transiently induce potentials via NMDA [63, 64], insulin has also been shown to impair NMDA dependent LTP [65]. Similarly, insulin may also attenuate AMPAR signaling by inducing AMPA receptor internalization [66]. However, the mechanism of action for these disparate actions of insulin needs to be understood in the context of the dynamics of intracellular signaling molecules like AMPK and mTORC.

AMPK may be critical in the low-energy response of neurons, both from an intraceullar and systems level perspective [27,67]. While AMPK is critical for the integration of inputs, mTORC is linked to protein translation and autophagy, which can serve as outputs for influencing cellular state. mTORC1, while active in presynaptic neurons, is not expressed as heavily in postsynaptic dendritic spines [31]. mTORC2, is expressed in dendritic spines and activated

during synaptic signaling [31, 67, 68]. There are additional reports that mTORC2 is essential for synaptic plasticity [31,69]. Due to the importance of insulin signaling and AMPK, further investigation of the kinetics of mTOR is vital for our understanding of cellular interactions leading to synaptic plasticity.

Future works in both modeling and experiments may focus more on building upon knowledge of synaptic plasticity. For modeling complex biochemical pathways, deterministic solver methods are feasible due to high molecule numbers [70]. However, incorporating stochastic solver methods may be able to capture biological behavior, which is particularly important in multi-scale problems like dendritic spines [3, 71] Finally, multivariate experimental measurements in spines during synaptic activity would be need to constrain the models and test model predictions.

Acknowledgments

The authors would like to acknowledge Maria Hernández Mesa, Guadalupe Garcia, and Lingxia Qiao for their feedback and discussion. Additionally, we acknowledge biorender.com for tools used to generate graphics in Figure 1. Finally, this work was supported by the University of California, San Diego Interfaces Graduate Training Program, Air Force Office of Scientific Research (AFOSR) Multidisciplinary University Research Initiative (MURI) grant FA9550-18-10051.

Tables

Table 1: AMPK, mTOR, and Metabolism Reactions

Rx	Reaction	Flux Equation	Note	Ref
A01	$ATP \rightarrow ADP$	$k_{HYD}ATP$	Hydrolysis	[72]
A02	$ADP \rightarrow ATP$	$\frac{VmaxOP*(ADP/KADP)^nH}{1+(ADP/KADP)^{nH}}$	Oxidative Phosphorylation	[72]
A03	$ADP + PCr \rightarrow ATP + Cr$	$\frac{VforCK*ADP*PCr/(Kia*Kb)}{1+\frac{ADP}{Kia}+\frac{PCr}{Kib}+\frac{ATP}{Kiq}+(ADP*\frac{PCr}{Kia*Kb})+((TCr-PCr)*\frac{ATP}{Kiq*Kp})}$	Creatine Kinase	[72]
A04	$ATP + Cr \rightarrow ADP + PCr$	$\frac{vCKr*ATP*(TCr-PCr)/(Kiq*Kp)}{1+\frac{ADP/Kia}{+}\frac{(PCr}{Kib}+\frac{ATP}{Kiq})+(ADP\frac{PCr}{(Kia*Kb})+((TCr-PCr)*\frac{ATP}{Kiq*Kp})}$	Creatine Kinase, Reverse	[72]
A05f	$ADP + ADP \rightarrow ATP + AMP$	$\frac{vAK*ATP*(AMP)/(kmt*kmm)}{1+(ATP/kmt)+(AMP/kmm)+(ATP*AMP/(kmt*kmm))+(2*ADP/kmd)+(ADP^2/kmd^2)}$	Adenylate Kinase	[72]
A05r	$ATP + AMP \rightarrow ADP + ADP$	$\frac{VrevAK*ADP^2/kmd^2}{1+(ATP/kmt)+(AMP/kmm)+(ATP*AMP/(kmt*kmm))+(2*ADP/kmd)+(ADP^2/kmd^2)}$	Adenylate Kinase	[72]
A06	$AMP + AMPK \rightarrow ATP + pAMPK$	$k_{fAMPK}AMPAMPK - k_{rAMPK}ATPpAMPK$	AMPK act. Reaction	[72]
A07	$AKT \rightarrow pAKT$	$\frac{V_{pAKT}*pAKT}{K_{m,pAKT}+pAKT}$	AKT Basal act.	[26]
A08	$pAKT \rightarrow AKT$	$\frac{K_{AKTpmTOR}*pmTORC2*AKT}{K_{m,AKT-pmTOR}+AKT}$	AKT Deact. by mTORC2	[26]
A09	$pmTORC1 \rightarrow mTORC1$	$\frac{K_{pmTORC1}+K_{pmTORC1AMPK}*pAMPK*pmTORC1}{K_{mpmTORC1A}+pmTORC1}$	mTORC1 deact. by AMPK	[26]
A10	$pmTORC1 \rightarrow mTORC1$	$\frac{K_{pmTORC1ULK1}*pULK1*pmTORC1}{K_{m,pmTORULK}+pmTORC1}$	mTORC1 deact. by ULK1	[26]
A11	$pmTORC1 \rightarrow mTORC1$	$\frac{K_{MAKT}*pAKT*mTORC1}{K_{m,MAKT}+mTORC1}$	mTORC1 act. by AKT	[26]
A12	$mTORC1 + DEP \rightarrow mTORC1 - DEP$	$K_{fDEP1} * mTORC1 * DEP - KrDEP1 * mTORC1 - DEP$	mTORC1 binding by DEP	[26]
A13	$pmTORC2 \rightarrow mTORC2$	$\frac{V_{mTORC2}*pmTORC2}{Km_{pmTORC2}+pmTORC2}$	mTOR basal deact.	[26]
A14	$mTORC2 \rightarrow pmTORC2$	$\frac{k_{M2AMPK}*pAMPK*mTORC2}{K_{m,m2AMPK}+mTORC2}$	mTORC2 act. by AMPK	[26]
A15	$mTORC2 + DEP \rightarrow mTORC2 - DEP$	$K_{f,DEP2} * mTORC2 * DEP - KrDEP2 * mTORC2 - DEP$	mTORC2 binding by DEP	[26]
A16	$pDEP \rightarrow DEP$	$\frac{V_{pDEP}*pDEP}{K_{m,pDEP}+pDEP}$	DEP dephos.	[26]
A17	$DEP \rightarrow pDEP$	$\frac{K_{DEPM1}*pmTORC1*DEP}{K_{m,DEPM1}+DEP}$	DEP act. with mTORC1	[26]
A18	$DEP \rightarrow pDEP$	$\frac{K_{DEPM2}*pmTORC2*DEP}{K_{m,DEPM2}+DEP}$	DEP act. with mTORC2	[26]
A19	$pAMPK \rightarrow AMPK$	$\frac{K_{pAMPK}+K_{pAMPKULK}*pULK1*pAMPK}{K_{m,pAMPK}+pAMPK}$	AMPK deact. by ULK1	[26]
A20	$pAMPK \rightarrow AMPK$	$\frac{K_{pAMPKM1}*pmTORC1*pAMPK}{K_{m,pAMPK}+pAMPK}$	AMPK deact. by mTORC1	[26]
A21	$AMPK \rightarrow pAMPK$	$\frac{K_{AMPK}+KAMPKSIRT*SIRT1*AMPK}{Km,AMPK+AMPK}$	AMPK act. by SIRT1	[26]
A22	$\rightarrow SIRT$	$\frac{K_{SIRT1}+KSIRT1_A*pAMPK*SIRT1_T-SIRT1}{K_{m,SIRT1}+SIRT1_T-SIRT1}$	SIRT act. by AMPK	[26]
A23	$ULK1 \rightarrow pULK1$	$\frac{K_{pULK1}+KpULK1m1*pmTORC1*pULK1}{K_{mpULK1}+pULK1}$	ULK act. by mTORC1	[26]
A24	$pULK1 \rightarrow ULK1$	$\frac{K_{ULK1}+KULK1AMPK*pAMPK*ULK1}{K_{mULK1}+ULK1}$	ULK deact. by AMPK	[26]
A25	$AKT \rightarrow pAKT$	$\frac{IRS*v_{akti}*AKT}{k_{m-akt-i}+AKT}$	Basal IRS act. of AKT	[26]
A26	$mTORC2 \rightarrow pmTORC2$	$\frac{IRS*v_{mtori}*mTORC2}{k_{m-mtor-i}+mTORC2}$	Basal IRS act. mTORC2	[26]

Table 2: Calcium Submodel Reactions

Reaction No.	**Reaction**	**Flux**	**Parameters**	**Citation**	**Note**
B1	$Ca_c^{2+} + ATP_e \rightarrow Ca_e^{2+}$	$J_{SERCA} = V_{SERCA} \frac{Ca_c^2}{K_p^2 + Ca_c^2} \frac{ATP_e}{K_{ds} + ATP_e}$		[73]	
B2	$Ca_e^{2+} \rightarrow Ca_c^{2+}$	$J_{IP_3R} = (k_{IP} b + k_{IP} IPR_{act})(Ca_e^{2+} - Ca_c^{2+})$	$K_f = 10, \gamma = 10$	[73]	IPR (Table 3)
B3	$\phi \rightarrow Ca_c$	$J_{NMDA} = g_{NMDA} NMDA_O \frac{1}{1+(e^{0.092V})*0.28}$		[49]	NMDA
B4	$\phi \rightarrow Ca_c^{2+}$	$J_{RYR} = (V_{RYR} P_O + V_{leak})(Ca_e^{2+} - Ca_c^{2+})$		[74]	Ryanodine
B5	$Ca_c^{2+} + ATP_e \rightarrow \phi$	$J_{PMCA} = V_{PMCA} \frac{Ca_c^2}{K_p^2 + Ca_c^2}$		[75]	PMCA
B6	$B + Ca_c^{2+} \rightarrow BCa_c^{2+}$	$J_{Buff} = k_{Buff}(Ca_c B - k_{eq,Buff} BCa)$		[76]	Buffering

Table 3: PSD Receptor Submodel Reactions

Receptor Species	Equation	Flux	Refs
NMDA			
$NMDA_U$	$\frac{dU}{dt} = -J_{N1}$	$J_{N1} = k_{1f}[Glut][U] - k_{1r}[M]$	[49]
$NMDA_M$	$\frac{dM}{dt} = -J_{N2}$	$J_{N2} = k_{2f}[Glut][M] - k_{2r}[C3]$	[49]
$NMDA_{C3}$	$\frac{dC3}{dt} = J_{N2} - J_{N3} - J_{N6}$	$J_{N3} = k_{3f}[C3] - k_{3r}[C2]$	[49]
$NMDA_{C2}$	$\frac{dC2}{dt} = J_{N3} - J_{N4} - J_{N7}$	$J_{N4} = k_{4f}[C2] - k_{4r}[C1]$	[49]
$NMDA_{C1}$	$\frac{dC1}{dt} = J_{N4} - J_{N5}$	$J_{N5} = k_{5f}[C1] - k_{5r}[O]$	[49]
$NMDA_D1$	$\frac{dD1}{dt} = J_{N6}$	$J_{N6} = k_{6f}[C3] - k_{6r}[D1]$	[49]
$NMDA_D2$	$\frac{dD2}{dt} = J_{N7}$	$J_{N7} = k_{7f}[C2] - k_{7r}[D2]$	[49]
$NMDA_O$	$\frac{dO}{dt} = J_{N5}$	$J_{N8} = k_{8f}[C1] - k_{8r}[O]$	[49]
mGluR			
R_2	$\frac{d[R_2]}{dt} = J_{LR}$	$J_{LR} = -k_b R_2 G^2 + k_u DIM$	[41]
DIM	$\frac{d[DIM]}{dt} = J_{DIM}$	$J_{DIM} = V_P \frac{DIM_p}{K_{mP}+DIM_p} - V_{PKC} \frac{PKC \cdot DIM}{K_{mPKC}+DIM}$	[41]
DIM_p	$\frac{d[DIM_p]}{dt} = J_{DIM_p}$	$J_{DIM_p} = \frac{R_{tot} - \sqrt{K_{dim} R_2} - 2R_2 - 2DIM}{2}$	[41]
DAG	$\frac{d[DAG]}{dt} = J_{DAG}$	$J_{DAG} = \frac{dPKC}{dt} = k_{aPKC} \frac{DAG}{K_{mDAG}+DAG}(1 - PKC) - k_{dPKC} PKC$	[41]
IP_3	$= \frac{d[IP_3]}{dt} J_{IP_3} = k_{PLC_I} DIM$		[41]
$AMPAR_U$	$\frac{dU}{dt} = -J_{A1}$	$J_{A1} = k_{A1f}[Glut][U] - k_{A1r}[M]$	[49]
$AMPAR_M$	$\frac{dM}{dt} = J_{A1} - J_{A2} - J_{A4}$	$J_{A2} = k_{A2f}[Glut][M] - k_{A2r}[C]$	[49]
$AMPAR_C$	$\frac{dC}{dt} = J_{A2} - J_{A3} - J_{A5}$	$J_{A3} = k_{A3f}[C] - k_{A3r}[O]$	[49]
$AMPAR_O$	$\frac{dO}{dt} = J_{A3} - J_{A6}$	$J_{A4} = k_{A4f}[M] - k_{A4r}[D1]$	[49]
$AMPAR_{D1}$	$\frac{dD1}{dt} = J_{A4} - J_{A7}$	$J_{A5} = k_{A5f}[C] - k_{A5r}[D2]$	[49]
$AMPAR_{D2}$	$\frac{dD2}{dt} = J_{A5} + J_{A7} - J_{A8}$	$J_{A6} = k_{A6f}[O] - k_{A6r}[D]$	[49]
$AMPAR_{D3}$	$\frac{dD3}{dt} = J_{A6} + J_{A8}$	$J_{A7} = k_{A7f}[D1][Glut] - k_{A7r}[D2]$	[49]
		$J_{A8} = k_{A8f}[D2] - k_{A8r}[D3]$	[49]
Voltage	$V = -65 + EPSP_A + EPSP_N + BPAP_A$		[3]
$EPSP_A$	$EPSP_A = [AMPA_O] G_{AMPA} V(t - \delta t) - V_{E,AMPA}$		[7]
$EPSP_N$	$EPSP_N = [NMDA_O] G_{NMDA} V(t - \delta t) - V_{E,NMDA} B(V((t - \delta t)))$		[7]
B(V)	$B(v) = \frac{1}{1 - \exp - K_m V \frac{Mg^{2+}}{3.27}}$		[7]

Table 4: Parameter Table

#	Parameter	Value	Ref	#	Parameters	Value	Ref
	Calcium Module						
31	$k1$	30	[73]	**32**	b	0.001	[73] [Altered]
33	Ki	5 $[\mu M]$	[74]	34	Ka	3 $[\mu M]$	[74]
35	IRa	EQN	[73]	36	k_{-}	0.02 $[1/s]$	[73]
37	k	20 $[1/uM^4s]$	[74]	38	V_{DAG}	0.0325 $[1/uM]$	[74]
39	kb	0.1 $[1/uM^2s]$	[41]	40	ku	2 $[1/s]$	[41]
41	Vp	0.05 $[UM/s]$	[41]	42	Kmp	5×10^{-4} $[uM]$	[41]
43	$Vpkc$	0.2 $[uM/s]$	[41]	44	$Kmpkc$	5×10^{-4} $[uM]$	[41]
45	$kapkc$	0.2 $[1/s]$	[41]	46	$kdpkc$	20 $[1/s]$	[41]
47	$kplcI$	3 $[1/s]$	[41]	48	$kplcD$	3 $[1/s]$	[41]
49	$KmDAG$	6 $[uM]$	[41]	50	$VRYR$	0.0050 $[1/s]$	[74]
51	Kar	0.0192 $[1/s]$	[74]	52	Kbr	0.2573 $[1/s]$	[74]
53	Kcr	0.0571 $[1/s]$	[74]	54	Kdr	0.1 $[1/s]$	[74]
55	V_{SERCA}	120 $[\mu M/s]$	[**?**]	56	$KpSERCA$	6 $[\mu M]$	[**?**]
74	Km_{ext}	0.1 $[\mu M^2]$	[75]	75	k_{deg}	5 $[1/s]$	[73]
76	$kpmleak$	0.5 $[1/s]$	[75]	77	k_{bcaf}	0.1 $[1/(\mu Ms)]$	[1]
78	k_{bcar}	1 $[1/s]$	[1]	79	k_{ERBf}	50 $[1/(\mu Ms)]$	[76]
80	k_{ERBr}	3 $[1/s]$	[76]	81	ker_{leak}	0.1 $[1/s]$	[To Sustain]
99	k_{cam_f}	0.001 $[1/(\mu Ms)]$	[76]	100	k_{cam_r}	1 $[1/s]$	[76]
101	Vm_{kk2}	0.01 $[\mu M/s]$	[77]	102	Km_{kk2}	0.01 $[\mu M]$	[77]
103	Ka_{kk2}	0.005 $[\mu M]$	[77]	104	$kf_{CaMDisc}$	1 $[1/s]$	[76]

Table 5: Parameter Table

#	Parameter	Value	Ref	#	Parameters	Value	Ref
	PSD Module						
57	Rb	$5 \quad 1/(\mu Ms)]$	[49]	58	Ru	$46.5 \quad [1/s]$	[49]
59	Rd	$8.4 \quad [1/s]$	[49]	60	Rr	$6.8 \quad [1/s]$	[49]
61	Ro	$46.5 \quad [1/s]$	[49]	62	Rc	$73.8 \quad [1/s]$	[49]
63	τ_{ess}	$0.05 \quad [s]$	[7]	64	τ_{esf}	$0.005 \quad [s]$	[7]
65	τ_{bss}	$0.025 \quad [s]$	[7]	66	τ_{bsf}	$0.003 \quad [s]$	[7]
67	$\tau_{delay,bp}$	$0.002 \quad [s]$	[7]	68	s	$10 \quad [mV]$	[7]
69	V_{rev}	$-65 \quad [mV]$	[3]	70	N_{NMDA}	1	[49]
71	$BPAP_{max}$	$40 \quad [mV]$	[7]	72	G_{NMDA}	$-65.6 \times 10^{-6} \quad [nS]$	[7]
73	k_{ext}	$1.3 \times 10^{-6} \quad [1/s]$	[Altered] [75]	82	G_{AMPA}	$15 \quad [nS]$	[7]
83	$kAMPA_{1f}$	$1.8 \quad [1/(\mu Ms)]$	[49]	84	$kAMPA_{2f}$	$10 \quad [1/(\mu Ms)]$	[49]
85	$kAMPA_{3f}$	$1.6 \times 10^{-4} \quad [1/s]$	[49]	86	$kAMPA_{4f}$	$7 \times 10^{2} \quad [1/s]$	[49]
87	$kAMPA_{5f}$	$1 \times 10^{2} \quad [1/s]$	[49]	88	$kAMPA_{6f}$	$3 \times 10^{2} \quad [1/s]$	[49]
89	$kAMPA_{7f}$	$10 \quad [1/s]$	[49]	90	$kAMPA_{8f}$	$1.6 \times 10^{4} \quad [1/s]$	[49]
91	$kAMPA_{1r}$	$2.4 \times 10^{3} \quad [1/s]$	[49]	92	$kAMPA_{2r}$	$1 \times 10^{4} \quad [1/s]$	[49]
93	$kAMPA_{3r}$	$5 \times 10^{3} \quad [1/s]$	[49]	94	$kAMPA_{4r}$	$1.5 \times 10^{2} \quad [1/s]$	[49]
95	$kAMPA_{5r}$	$2.1 \quad [1/s]$	[49]	96	$kAMPA_{6r}$	$15 \quad [1/s]$	[49]
97	$kAMPA_{7r}$	$1 \times 10^{3} \quad [1/s]$	[49]	98	$kAMPA_{8r}$	$1.2 \times 10^{4} \quad [1/s]$	[49]

Table 6: Parameter Table

#	Parameter	Value	Ref	#	Parameters	Value	Ref
	ATP Energetics						
1	K_{ADP}	$500 \quad [\mu M]$	[72]	**2**	$VmaxOP$	$0.5 \quad [mM/s]$	[72]
3	nH	2.568	[72]	**4**	k_{HYD}	$2.6 \times 10^{-2} \quad [mM/s]$	[72]
7	vAK	$14.66 \quad [mM/s]$	[72]	8	kmt	$0.27 \quad [mM]$	[72]
9	kmd	$0.35 \quad [mM]$	[72]	10	kmm	$0.32 \quad [mM]$	[72]
11	$keqadk$	0.744	[72]	12	$vmax20$	$2 \times 10^{-2} \quad [mM/s]$	[72]
13	$vmax21$	1×10^{-4}	[72]	14	$km20$	$1.4 \quad [mM]$	[72]
15	$km21$	$6.7 \times 10^{-2} \quad [mM]$	[72]	16	$k12f$	$1 \quad [1/(mMs)]$	[72]
17	$k12r$	$1.82 \times 10^{-2} \quad [1/s]$	[72]	18	$k13f$	$1 \quad [1/(mMs)]$	[72]
19	$k13r$	$1.82 \times 10^{-2} \quad [1/s]$	[72]	20	$kaicar$	$4 \times 10^{-4} \quad [1/s]$	[72]
21	$kAKT$	$3 \times 10^{-3} \quad [1/s]$	[72]	22	$kcatAMPK$	$34.56 \quad [1/s]$	[72]
23	V_CK	1×10^{2}	[72]	24	Kb	$1.11 \quad [mM]$	[72]
25	Kia	$0.135 \quad [mM]$	[72]	26	Kib	$3.9 \quad [mM]$	[72]
27	Kiq	$3.5 \quad [mM]$	[72]	28	$Kp(ATP)$	$3.8 \quad [mM]$	[72]
29	$KeqCK$	1.77×10^{2}	[72]	30	TCr	$39 \quad [mM]$	[72]

Supplementary Figures

Table 7: Parameter Table

#	Parameter	Value	Ref	#	Parameters	Value	Ref
	mTOR Module						
105	V_{IR}	9.67 $[nM/s]$	[26]	**106**	Km_{IR}	94.9 $[nM/s]$	[26]
107	V_{pIR}	26.2 $[nM/s]$	[26]	**108**	Km_{pIR}	35.0 $[nM]$	[26]
109	K_{IRSpIR}	3.57 $[1/s]$	[26]	**110**	Km_{IRSpIR}	50.1 $[nM]$	[26]
111	V_{pIRS}	18.4 $[1/s]$	[26]	**112**	Km_{pIRS}	50.0 $[nM]$	[26]
113	$K_{AKT,IRS}$	1.243 $[1/s]$	[26]	**114**	$Km_{AKT,IRS}$	6.27 $[nM]$	[26]
115	$K_{AKT,pM2}$	0.564 $[1/s]$	[26]	**116**	$Km_{AKT,pM2}$	5.23 $[nM]$	[26]
117	V_{pAKT}	16.2 $[nM/s]$	[26]	**118**	Km_{pAKT}	33.6 $[nM]$	[26]
119	$Km_{pM1,pAKT}$	0.594 $[1/s]$	[26]	**120**	$K_{pM1,pAKT}$	2.32 $[1/s]$	[26]
121	K_{pm1}	50.2 $[1/s]$	[26]	**122**	$K_{pM1,pAMPK}$	0.0238 $[1/s]$	[26]
123	$Km_{pM1,pAMPK}$	2.14 $[nM]$	[26]	**124**	$K_{pM1,ULK}$	0.0113 $[1/s]$	[26]
125	$Km_{pM1,ULK}$	1.99 $[nM]$	[26]	**126**	$K_{M2,IRS}$	13.3 $[1/s]$	[26]
127	$Km_{M2,IRS}$	160 $[nM]$	[26]	**128**	$K_{M2,pAMPK}$	1.57 $[1/s]$	[26]
129	$Km_{M2,pAMPK}$	160 $[nM]$	[26]	**130**	$V_{pmTORC2}$	25.4 $[nM/s]$	[26]
131	$Km_{pmTORC2}$	8.20 $[nM]$	[26]	132	K_{DEPM1}	0.995 $[1/s]$	[26]
133	Km_{DEPM1}	120.1 $[nM]$	[26]	134	K_{DEPM2}	0.279 $[1/s]$	[26]
135	Km_{DEPM2}	10.6 $[nM]$	[26]	136	$V_{pDEPTOR}$	54.1 $[nM/s]$	[26]
137	$Km_{pDEPTOR}$	8.23 $[nM]$	[26]	138	K_{M1DEPf}	0.0163 $[1/s]$	[26]
139	K_{M1DEPd}	0.120 $[1/s]$	[26]	**140**	K_{M2DEPf}	0.144 $[1/s1/s]$	[26]
141	K_{M2DEPd}	0.120 $[1/s]$	[26]	**142**	$K_{IRS,iIRS}$	1.84 $[1/s]$	[26]
143	$Km_{IRS,iIRS}$	50.1 $[nM]$	[26]	**144**	V_{iIRS}	13.5 $[nM/s]$	[26]
145	Km_{iIRS}	50.1 $[nM]$	[26]	146	K_{AMPK}	100 $[1/s]$	[26]
147	$K_{AMPK,SIRT1}$	84.3 $[1/s]$	[26]	148	Km_{AMPK}	124 $[nM]$	[26]
149	K_{pAMPK}	22.4 $[1/s]$	[26]	150	$K_{pAMPK,pULK1}$	473 $[1/s]$	[26]
151	$K_{pAMPK,pmTORC1}$	18.9 $[1/s]$	[26]	152	Km_{pAMPK}	100 $[nM]$	[26]
153	K_{SIRT1}	2.32 $[1/s]$	[26]	154	$K_{SIRT1,pAMPK}$	0.727 $[1/s]$	[26]
155	Km_{SIRT1}	3.77 $[nM]$	[26]	156	$K_{SIRT1,r}$	0.502 $[1/s]$	[26]
157	K_{ULK1}	39.2 $[1/s]$	[26]	**158**	$K_{ULK1,pAMPK}$	2.05 $[1/s]$	[26]
159	Km_{ULK1}	98.9 $[nM]$	[26]	160	K_{pULK1}	0.131 $[1/s]$	[26]
161	$K_{pULK1,pmTORC1}$	6.00 $[1/s]$	[26]	162	Km_{pULK1}	23.5 $[nM]$	[26]

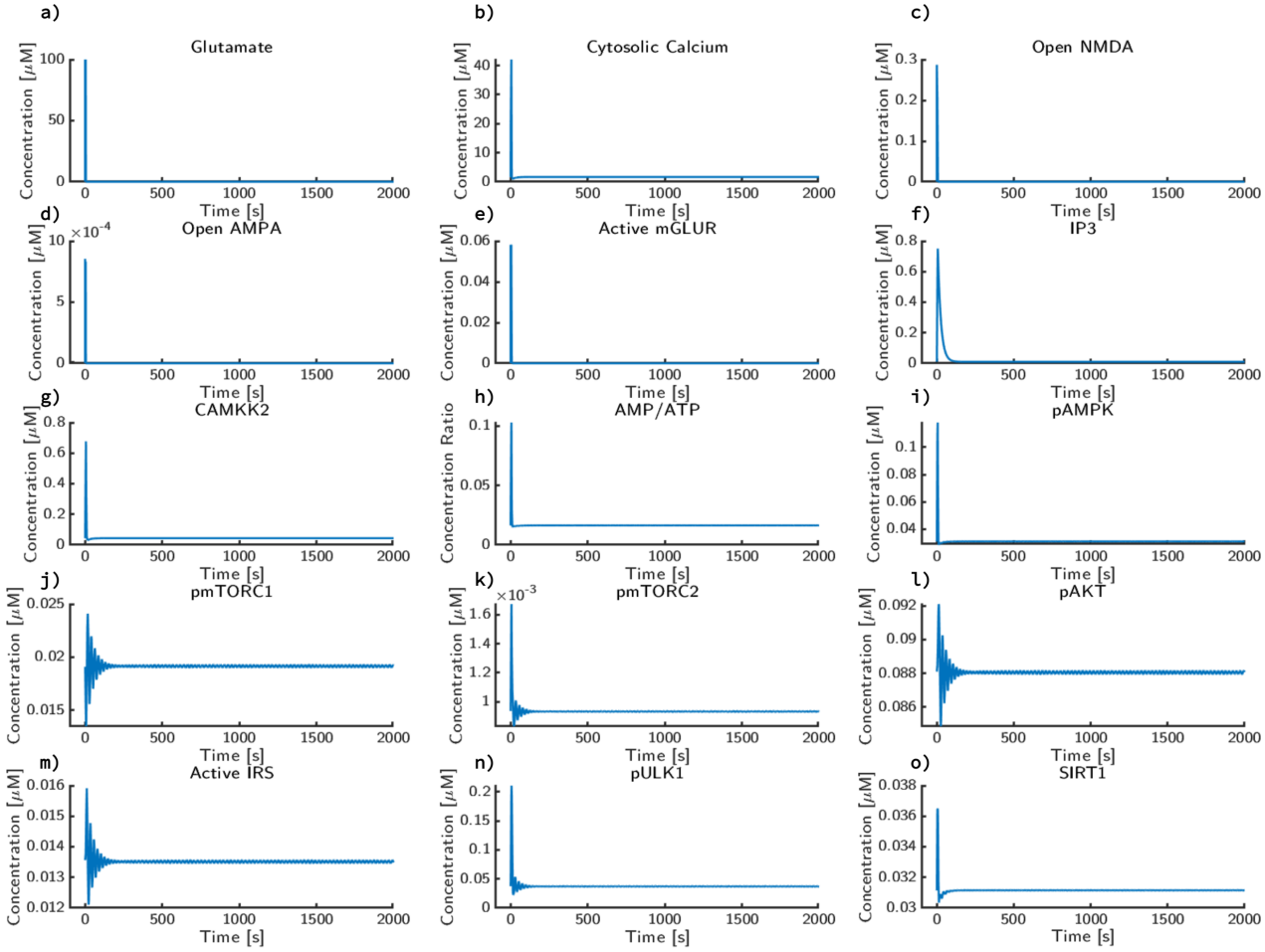

Supplemental Figure 1: **Equilibration simulation for system without glutamatergic stimulus.** The system recieved a single pulse of glutamate and was allowed to equilibrate for 2000 seconds. Trajectories are plotted for:**a)** glutamate, **b)** cytosolic calcium, **c)** open NMDA Receptors, **d)** open AMPA receptors, **e)** active mGLUR receptor, **f)** IP3, **g)** CAMKK2, **h)** AMP/ATP ratio, **i)** phosphorylated AMPK, **j)** phosphorylated mTORC1, **k)** phosphorylated mTORC2, **l)** phosphorylated AKT, **m)** active IRS, **n)** phosphorylated ULK1, **o)** SIRT1.

Competing Interests

References

[1] M. Bell, T. Bartol, T. Sejnowski, and P. Rangamani, "Dendritic spine geometry and spine apparatus organization govern the spatiotemporal dynamics of calcium," *J. Gen. Physiol.*, vol. 151, pp. 1017–1034, Aug. 2019.

[2] M. K. Bell, M. V. Holst, C. T. Lee, and P. Rangamani, "Dendritic spine morphology regulates calcium-dependent synaptic weight change." May 2022.

[3] T. M. Bartol, D. X. Keller, J. P. Kinney, C. L. Bajaj, K. M. Harris, T. J. Sejnowski, and M. B. Kennedy, "Computational reconstitution of spine calcium transients from individual proteins," *Front. Synaptic Neurosci.*, vol. 7, p. 17, Oct. 2015.

[4] M. K. Bell, C. T. Lee, and P. Rangamani, "Spatiotemporal modeling reveals geometric dependence of AMPAR dynamics on dendritic spine morphology." June 2022.

[5] J. Lisman, R. Yasuda, and S. Raghavachari, "Mechanisms of CaMKII action in long-term potentiation," *Nat. Rev. Neurosci.*, vol. 13, pp. 169–182, Feb. 2012.

[6] R. S. Zucker, "Calcium- and activity-dependent synaptic plasticity," *Curr. Opin. Neurobiol.*, vol. 9, pp. 305–313, June 1999.

[7] H. Z. Shouval, M. F. Bear, and L. N. Cooper, "A unified model of NMDA receptor-dependent bidirectional synaptic plasticity," *Proc. Natl. Acad. Sci. U. S. A.*, vol. 99, pp. 10831–10836, Aug. 2002.

[8] J. C. Magee and C. Grienberger, "Synaptic plasticity forms and functions," *Annu. Rev. Neurosci.*, vol. 43, pp. 95–117, July 2020.

[9] J. Karbowski, "Metabolic constraints on synaptic learning and memory," *J. Neurophysiol.*, vol. 122, pp. 1473–1490, Oct. 2019.

[10] G. C. Garcia, T. M. Bartol, S. Phan, E. A. Bushong, G. Perkins, T. J. Sejnowski, M. H. Ellisman, and A. Skupin, "Mitochondrial morphology provides a mechanism for energy buffering at synapses," *Sci. Rep.*, vol. 9, p. 18306, Dec. 2019.

[11] W. B. Potter, K. J. O'Riordan, D. Barnett, S. M. K. Osting, M. Wagoner, C. Burger, and A. Roopra, "Metabolic regulation of neuronal plasticity by the energy sensor AMPK," *PLoS One*, vol. 5, p. e8996, Feb. 2010.

[12] D. Attwell and S. B. Laughlin, "An energy budget for signaling in the grey matter of the brain," *J. Cereb. Blood Flow Metab.*, vol. 21, pp. 1133–1145, Oct. 2001.

[13] J. J. Harris, R. Jolivet, and D. Attwell, "Synaptic energy use and supply," *Neuron*, vol. 75, pp. 762–777, Sept. 2012.

[14] E. Engl, R. Jolivet, C. N. Hall, and D. Attwell, "Non-signalling energy use in the developing rat brain," *J. Cereb. Blood Flow Metab.*, vol. 37, pp. 951–966, Mar. 2017.

[15] G. A. Dienel, "Brain glucose metabolism: Integration of energetics with function," *Physiol. Rev.*, vol. 99, pp. 949–1045, Jan. 2019.

[16] G. Yellen, "Fueling thought: Management of glycolysis and oxidative phosphorylation in neuronal metabolism," *J. Cell Biol.*, vol. 217, pp. 2235–2246, July 2018.

[17] O. Kann and R. Kovács, "Mitochondria and neuronal activity," *Am. J. Physiol. Cell Physiol.*, vol. 292, pp. C641–57, Feb. 2007.

[18] J. M. Ferreira, A. L. Burnett, and G. A. Rameau, "Activity-dependent regulation of surface glucose transporter-3," *J. Neurosci.*, vol. 31, pp. 1991–1999, Feb. 2011.

[19] V. Rangaraju, M. Lauterbach, and E. M. Schuman, "Spatially stable mitochondrial compartments fuel local translation during plasticity," *Cell*, vol. 176, pp. 73–84.e15, Jan. 2019.

[20] C. M. Díaz-García, D. J. Meyer, N. Nathwani, M. Rahman, J. R. Martínez-François, and G. Yellen, "The distinct roles of calcium in rapid control of neuronal glycolysis and the tricarboxylic acid cycle," *Elife*, vol. 10, Feb. 2021.

[21] G. C. Garcia, T. M. Bartol, and T. J. Sejnowski, "A thermodynamically-consistent model for ATP production in mitochondria." Aug. 2022.

[22] G. Mairet-Coello, J. Courchet, S. Pieraut, V. Courchet, A. Maximov, and F. Polleux, "The CAMKK2-AMPK kinase pathway mediates the synaptotoxic effects of Aβ oligomers through tau phosphorylation," *Neuron*, vol. 78, pp. 94–108, Apr. 2013.

[23] C. Marinangeli, S. Didier, T. Ahmed, R. Caillerez, M. Domise, C. Laloux, S. Bégard, S. Carrier, M. Colin, P. Marchetti, B. Ghesquière, D. Balschun, L. Buée, J. Kluza, and V. Vingtdeux, "AMP-Activated protein kinase is essential for the maintenance of energy levels during synaptic activation," *iScience*, vol. 9, pp. 1–13, Nov. 2018.

[24] J. Adams, Z.-P. Chen, B. J. W. Van Denderen, C. J. Morton, M. W. Parker, L. A. Witters, D. Stapleton, and B. E. Kemp, "Intrasteric control of AMPK via the gamma1 subunit AMP allosteric regulatory site," *Protein Sci.*, vol. 13, pp. 155–165, Jan. 2004.

[25] K.-I. Kuwako and H. Okano, "Versatile roles of LKB1 kinase signaling in neural development and homeostasis," *Front. Mol. Neurosci.*, vol. 11, p. 354, Oct. 2018.

[26] M. Sadria, D. Seo, and A. T. Layton, "The mixed blessing of AMPK signaling in cancer treatments," *BMC Cancer*, vol. 22, p. 105, Jan. 2022.

[27] D. Kong, Y. Dagon, J. N. Campbell, Y. Guo, Z. Yang, X. Yi, P. Aryal, K. Wellenstein, B. B. Kahn, B. L. Sabatini, and B. B. Lowell, "A postsynaptic AMPK→p21-Activated kinase pathway drives Fasting-Induced synaptic plasticity in AgRP neurons," *Neuron*, vol. 91, pp. 25–33, July 2016.

[28] W. Dai, Y. Xu, S. Mo, Q. Li, J. Yu, R. Wang, Y. Ma, Y. Ni, W. Xiang, L. Han, L. Zhang, S. Cai, J. Qin, W.-L. Chen, W. Jia, and G. Cai, "GLUT3 induced by AMPK/CREB1 axis is key for withstanding energy stress and augments the efficacy of current colorectal cancer therapies," *Signal Transduct Target Ther*, vol. 5, p. 177, Sept. 2020.

[29] A. S. Marsin, L. Bertrand, M. H. Rider, J. Deprez, C. Beauloye, M. F. Vincent, G. Van den Berghe, D. Carling, and L. Hue, "Phosphorylation and activation of heart PFK-2 by AMPK has a role in the stimulation of glycolysis during ischaemia," *Curr. Biol.*, vol. 10, pp. 1247–1255, Oct. 2000.

[30] O. Watters, N. M. C. Connolly, H.-G. König, H. Düssmann, and J. H. M. Prehn, "AMPK preferentially depresses retrograde transport of axonal mitochondria during localized nutrient deprivation," *J. Neurosci.*, vol. 40, pp. 4798–4812, June 2020.

[31] M. P. McCabe, E. R. Cullen, C. M. Barrows, A. N. Shore, K. I. Tooke, K. A. Laprade, J. M. Stafford, and M. C. Weston, "Genetic inactivation of mTORC1 or mTORC2 in neurons reveals distinct functions in glutamatergic synaptic transmission," *Elife*, vol. 9, Mar. 2020.

[32] M. K. Seo, L. T. Hien, M. K. Park, A. J. Choi, D.-H. Seog, S.-H. Kim, S. W. Park, and J. G. Lee, "AMPA receptor-mTORC1 signaling activation is required for neuroplastic effects of LY341495 in rat hippocampal neurons," *Sci. Rep.*, vol. 10, p. 993, Jan. 2020.

[33] C. Garza-Lombó, A. Schroder, E. M. Reyes-Reyes, and R. Franco, "mTOR/AMPK signaling in the brain: Cell metabolism, proteostasis and survival," *Curr Opin Toxicol*, vol. 8, pp. 102–110, Apr. 2018.

[34] Y. Wang, M. F. Barbaro, and S. C. Baraban, "A role for the mTOR pathway in surface expression of AMPA receptors," *Neurosci. Lett.*, vol. 401, pp. 35–39, June 2006.

[35] E. Hu, A. Mergenthal, C. S. Bingham, D. Song, J.-M. Bouteiller, and T. W. Berger, "A glutamatergic spine model to enable Multi-Scale modeling of nonlinear calcium dynamics," *Front. Comput. Neurosci.*, vol. 12, p. 58, July 2018.

[36] A. Leung, D. Ohadi, G. Pekkurnaz, and P. Rangamani, "Deciphering the postsynaptic calcium-mediated energy homeostasis through mitochondria-endoplasmic reticulum contact sites using systems modeling." Sept. 2020.

[37] G. C. Castellani, E. M. Quinlan, L. N. Cooper, and H. Z. Shouval, "A biophysical model of bidirectional synaptic plasticity: dependence on AMPA and NMDA receptors," *Proc. Natl. Acad. Sci. U. S. A.*, vol. 98, pp. 12772–12777, Oct. 2001.

[38] R. Bertram, M. Gram Pedersen, D. S. Luciani, and A. Sherman, "A simplified model for mitochondrial ATP production," *J. Theor. Biol.*, vol. 243, pp. 575–586, Dec. 2006.

[39] N. M. C. Connolly, B. D'Orsi, N. Monsefi, H. J. Huber, and J. H. M. Prehn, "Computational analysis of AMPK-Mediated neuroprotection suggests acute excitotoxic bioenergetics and glucose dynamics are regulated by a minimal set of critical reactions," *PLoS One*, vol. 11, p. e0148326, Feb. 2016.

[40] K. D. Baker, T. M. Edwards, and N. S. Rickard, "The role of intracellular calcium stores in synaptic plasticity and memory consolidation," *Neurosci. Biobehav. Rev.*, vol. 37, pp. 1211–1239, Aug. 2013.

[41] G. Dupont, E. F. L. Lokenye, and R. A. J. Challiss, "A model for ca2+ oscillations stimulated by the type 5 metabotropic glutamate receptor: an unusual mechanism based on repetitive, reversible phosphorylation of the receptor," *Biochimie*, vol. 93, pp. 2132–2138, Dec. 2011.

[42] M. Segal and E. Korkotian, "Endoplasmic reticulum calcium stores in dendritic spines," *Front. Neuroanat.*, vol. 8, p. 64, July 2014.

[43] G. Ashrafi and T. A. Ryan, "Glucose metabolism in nerve terminals," *Curr. Opin. Neurobiol.*, vol. 45, pp. 156–161, Aug. 2017.

[44] P. Theurey, N. M. C. Connolly, I. Fortunati, E. Basso, S. Lauwen, C. Ferrante, C. Moreira Pinho, A. Joselin, A. Gioran, D. Bano, D. S. Park, M. Ankarcrona, P. Pizzo, and J. H. M. Prehn, "Systems biology identifies preserved integrity but impaired metabolism of mitochondria due to a glycolytic defect in alzheimer's disease neurons," *Aging Cell*, vol. 18, p. e12924, June 2019.

[45] R. Occhipinti, E. Somersalo, and D. Calvetti, "Energetics of inhibition: insights with a computational model of the human GABAergic neuron-astrocyte cellular complex," *J. Cereb. Blood Flow Metab.*, vol. 30, pp. 1834–1846, Nov. 2010.

[46] G. Le Masson, S. Przedborski, and L. F. Abbott, "A computational model of motor neuron degeneration," *Neuron*, vol. 83, pp. 975–988, Aug. 2014.

[47] D. A. Beard, "A biophysical model of the mitochondrial respiratory system and oxidative phosphorylation," *PLoS Comput. Biol.*, vol. 1, p. e36, Sept. 2005.

[48] J. D. Clements, R. A. Lester, G. Tong, C. E. Jahr, and G. L. Westbrook, "The time course of glutamate in the synaptic cleft," *Science*, vol. 258, pp. 1498–1501, Nov. 1992.

[49] Professor of Computation and Neural Systems Christof Koch, C. Koch, and I. Segev, *Methods in Neuronal Modeling: From Ions to Networks*. MIT Press, 1998.

[50] A. Öst, K. Svensson, I. Ruishalme, C. Brännmark, N. Franck, H. Krook, P. Sandström, P. Kjolhede, and P. Strålfors, "Attenuated mTOR signaling and enhanced autophagy in adipocytes from obese patients with type 2 diabetes," *Molecular Medicine*, vol. 16, pp. 235–246, Mar. 2010.

[51] MATLAB, *version 9.11.0 (R2021b)*. Natick, Massachusetts: The MathWorks Inc., 2021.

[52] J. Larson and E. Munkácsy, "Theta-burst LTP," *Brain Res.*, vol. 1621, pp. 38–50, Sept. 2015.

[53] L. M. Grover, E. Kim, J. D. Cooke, and W. R. Holmes, "LTP in hippocampal area CA1 is induced by burst stimulation over a broad frequency range centered around delta," *Learn. Mem.*, vol. 16, pp. 69–81, Jan. 2009.

[54] R. Heinrich, B. G. Neel, and T. A. Rapoport, "Mathematical models of protein kinase signal transduction," *Mol. Cell*, vol. 9, pp. 957–970, May 2002.

[55] B. W. Bernstein and J. R. Bamburg, "Actin-ATP hydrolysis is a major energy drain for neurons," *J. Neurosci.*, vol. 23, pp. 1–6, Jan. 2003.

[56] A. Lajtha, G. E. Gibson, G. A. Dienel, and G. A. Dienel, *Handbook of neurochemistry and molecular neurobiology: brain energetics. Integration of molecular and cellular processes*. Springer Science & Business Media, 2007.

[57] S. S. Divakaruni, A. M. Van Dyke, R. Chandra, T. A. LeGates, M. Contreras, P. A. Dharmasri, H. N. Higgs, M. K. Lobo, S. M. Thompson, and T. A. Blanpied, "Long-Term potentiation requires a rapid burst of dendritic mitochondrial fission during induction," *Neuron*, vol. 100, pp. 860–875.e7, Nov. 2018.

[58] R. C. Malenka, "The role of postsynaptic calcium in the induction of long-term potentiation," *Mol. Neurobiol.*, vol. 5, no. 2-4, pp. 289–295, 1991.

[59] M. Domise, F. Sauvé, S. Didier, R. Caillerez, S. Bégard, S. Carrier, M. Colin, C. Marinangeli, L. Buée, and V. Vingtdeux, "Neuronal AMP-activated protein kinase hyper-activation induces synaptic loss by an autophagy-mediated process," *Cell Death Dis.*, vol. 10, p. 221, Mar. 2019.

[60] J. Lappalainen, J. Herpich, and C. Tetzlaff, "A theoretical framework to derive simple, Firing-Rate-Dependent mathematical models of synaptic plasticity," *Front. Comput. Neurosci.*, vol. 13, p. 26, May 2019.

[61] G. C. Castellani, E. M. Quinlan, F. Bersani, L. N. Cooper, and H. Z. Shouval, "A model of bidirectional synaptic plasticity: from signaling network to channel conductance," *Learn. Mem.*, vol. 12, pp. 423–432, July 2005.

[62] C. R. Ferrario and L. P. Reagan, "Insulin-mediated synaptic plasticity in the CNS: Anatomical, functional and temporal contexts," *Neuropharmacology*, vol. 136, pp. 182–191, July 2018.

[63] L. Liu, J. C. Brown, 3rd, W. W. Webster, R. A. Morrisett, and D. T. Monaghan, "Insulin potentiates N-methyl-D-aspartate receptor activity in xenopus oocytes and rat hippocampus," *Neurosci. Lett.*, vol. 192, pp. 5–8, June 1995.

[64] V. A. Skeberdis, J. Lan, X. Zheng, R. S. Zukin, and M. V. Bennett, "Insulin promotes rapid delivery of N-methyl-D- aspartate receptors to the cell surface by exocytosis," *Proc. Natl. Acad. Sci. U. S. A.*, vol. 98, pp. 3561–3566, Mar. 2001.

[65] E. D. Martín, A. Sánchez-Perez, J. L. Trejo, J. A. Martin-Aldana, M. Cano Jaimez, S. Pons, C. Acosta Umanzor, L. Menes, M. F. White, and D. J. Burks, "IRS-2 deficiency impairs NMDA receptor-dependent long-term potentiation," *Cereb. Cortex*, vol. 22, pp. 1717–1727, Aug. 2012.

[66] E. C. Beattie, R. C. Carroll, X. Yu, W. Morishita, H. Yasuda, M. von Zastrow, and R. C. Malenka, "Regulation of AMPA receptor endocytosis by a signaling mechanism shared with LTD," *Nat. Neurosci.*, vol. 3, pp. 1291–1300, Dec. 2000.

[67] N. Belforte, J. Agostinone, L. Alarcon-Martinez, D. Villafranca-Baughman, F. Dotigny, J. L. Cueva Vargas, and A. Di Polo, "AMPK hyperactivation promotes dendrite retraction, synaptic loss, and neuronal dysfunction in glaucoma," *Mol. Neurodegener.*, vol. 16, p. 43, June 2021.

[68] T. Ma, N. Tzavaras, P. Tsokas, E. M. Landau, and R. D. Blitzer, "Synaptic stimulation of mTOR is mediated by wnt signaling and regulation of glycogen synthetase kinase-3," *J. Neurosci.*, vol. 31, pp. 17537–17546, Nov. 2011.

[69] N. Takei and H. Nawa, "mTOR signaling and its roles in normal and abnormal brain development," *Front. Mol. Neurosci.*, vol. 7, p. 28, Apr. 2014.

[70] S. K. Hahl and A. Kremling, "A comparison of deterministic and stochastic modeling approaches for biochemical reaction systems: On fixed points, means, and modes," *Front. Genet.*, vol. 7, p. 157, Aug. 2016.

[71] N. Hoze and D. Holcman, "Residence times of receptors in dendritic spines analyzed by stochastic simulations in empirical domains," *Biophys. J.*, vol. 107, pp. 3008–3017, Dec. 2014.

[72] I. F. Coccimiglio and D. C. Clarke, "ADP is the dominant controller of AMP-activated protein kinase activity dynamics in skeletal muscle during exercise," *PLoS Comput. Biol.*, vol. 16, p. e1008079, July 2020.

[73] B. Wacquier, L. Combettes, G. T. Van Nhieu, and G. Dupont, "Interplay between intracellular ca(2+) oscillations and ca(2+)-stimulated mitochondrial metabolism," *Sci. Rep.*, vol. 6, p. 19316, Jan. 2016.

[74] J. Keizer and L. Levine, "Ryanodine receptor adaptation and ca2+(-)induced ca2+ release-dependent ca2+ oscillations," *Biophys. J.*, vol. 71, pp. 3477–3487, Dec. 1996.

[75] E. A. Nimchinsky, "The Number of Glutamate Receptors Opened by Synaptic Stimulation in Single Hippocampal Spines," *Journal of Neuroscience*, vol. 24, pp. 2054–2064, Feb. 2004.

[76] B. K. Jha and A. Jha, "Two dimensional finite volume model to study the effect of ER on cytosolic calcium distribution in astrocytes," *Procedia Comput. Sci.*, vol. 46, pp. 1285–1293, Jan. 2015.

[77] A. Woods, K. Dickerson, R. Heath, S.-P. Hong, M. Momcilovic, S. R. Johnstone, M. Carlson, and D. Carling, "Ca2+/calmodulin-dependent protein kinase kinase-beta acts upstream of AMP-activated protein kinase in mammalian cells," *Cell Metab.*, vol. 2, pp. 21–33, July 2005.